

Tetrahedron deformation and alignment of perceived vorticity and strain in a turbulent flow

Alain Pumir,¹ Eberhard Bodenschatz,^{2,3,4} and Haitao Xu²

¹*Laboratoire de Physique, Ecole Normale Supérieure de Lyon, Université Lyon 1 and CNRS, F-69007 France*

²*Max Planck Institute for Dynamics and Self-Organization (MPIDS), Göttingen, D-37077 Germany*

³*Institute for Nonlinear Dynamics, University of Göttingen, D-37077 Germany*

⁴*Laboratory of Atomic and Solid State Physics and Sibley School of Mechanical and Aerospace Engineering, Cornell University, Ithaca, NY 14853, USA*

(Dated: 2 November 2018)

We describe the structure and dynamics of turbulence by the scale-dependent perceived velocity gradient tensor as supported by following four tracers, *i.e.* fluid particles, that initially form a regular tetrahedron. We report results from experiments in a von Kármán swirling water flow and from numerical simulations of the incompressible Navier-Stokes equation. We analyze the statistics and the dynamics of the perceived rate of strain tensor and vorticity for initially regular tetrahedron of size r_0 from the dissipative to the integral scale. Just as for the true velocity gradient, at any instant, the perceived vorticity is also preferentially aligned with the intermediate eigenvector of the perceived rate of strain. However, in the perceived rate of strain eigenframe fixed at a given time $t = 0$, the perceived vorticity evolves in time such as to align with the strongest eigendirection at $t = 0$. This also applies to the true velocity gradient. The experimental data at the higher Reynolds number suggests the existence of a self-similar regime in the inertial range. In particular, the dynamics of alignment of the perceived vorticity and strain can be rescaled by t_0 , the turbulence time scale of the flow when the scale r_0 is in the inertial range. For smaller Reynolds numbers we found the dynamics to be scale dependent.

I. INTRODUCTION

The fundamental question of how small scales are generated in turbulent flows is not fully understood¹. From a mathematical point of view, small scales are produced by the temporal amplification of the velocity gradients when following a fluid element²⁻⁴. While the velocity gradient tensor is in principle available in direct numerical simulations (DNS), the rare, very intense fluctuations of the gradients make it numerically very challenging to accurately determine their statistical properties⁵. In laboratory flows, of course the physics guarantees that all scales are resolved. However, measurements of the full velocity gradient tensor are in practice extremely difficult⁶⁻¹¹.

To address the question of the generation of small scales, one needs to know the evolution of the flow when following a fluid element. The recent development of Lagrangian measurement technology now allows one to experimentally investigate this issue⁹. Nevertheless, the precise measurement of the velocity *gradient* tensor at high Reynolds numbers will for the foreseeable future remain immensely challenging due to temporal and spatial resolution constraints.

Because of the difficulty in determining reliably the velocity gradient, a fruitful alternative approach consists in investigating a coarse-grained version of the velocity tensor over a region of size r_0 . In addition to the possibility of determining the flow evolution from a Lagrangian point of view, and thus of addressing fundamental questions about the generation of small scales, this approach enables the study of the scale dependence of flow properties, especially in the inertial range of scales where the dynamics is believed to be determined by inertia only, and dissipation can be considered as negligible. Several approaches can be used to define a coarse-grained velocity gradient tensor. One method consists in measuring the true coarse-grained tensor by averaging the velocity gradients over a well resolved region^{7,12}. The alternative strategy followed in this work rests on a reduced description^{13,14}, based on defining a “perceived velocity gradient tensor” (denoted from now on by $\mathbf{M}(t)$ or $M_{ij}(t)$) that is supported only by four fluid elements, initially separated by a distance r_0 from each other, thus forming a regular tetrahedron. The tensor $\mathbf{M}(t)$ reduces to the true velocity gradient tensor $\mathbf{m}(t)$ when $r_0 \rightarrow 0$, or more precisely, when the scale r_0 is much smaller than the Kolmogorov scale, η , the smallest length scale in the flow. One physically important feature of this description is that it provides insight not only on \mathbf{M} , but also on the geometry, *i.e.*, the shape of the tetrahedron, and on its time evolution. As we see later, the two aspects are strongly coupled^{13,14}. Thus,

the approach based on the perceived velocity gradient tensor and its evolution significantly differs from the one based on the true coarse-grained velocity gradient¹⁵. From a theoretical point of view, the description used here replaces a continuous field by a relatively small number of degrees of freedom. It is one of the hopes of the present approach that such a conceptual simplification could help in devising simple tractable models, which would help shed new light on turbulence.

The velocity gradient tensor has been shown to possess the property that instantaneously vorticity aligns with the *intermediate* stretching direction (eigenvector) of the rate of strain tensor^{6,16–18}, whose eigenvalue is predominantly positive. This was surprising as vorticity was expected to align with the *strongest* stretching direction. Already Taylor conjectured^{1,19} that the turbulent cascade mechanism relies on the amplification of vortices of scale r_0 by stretching that subsequently leads to breakup of the vortices into smaller ones. Our recent results¹⁴ provide new insight on this conjecture. By analyzing the time evolution of tetrahedra of size r_0 , we found that the perceived vorticity tends to align with the earlier direction of the *strongest* stretching, corresponding to the largest eigenvalue of the perceived rate of strain tensor. For r_0 in the inertial range, this evolution depended only on t/t_0 , where $t_0 \equiv (r_0^2/\varepsilon)^{1/3}$ is the time scale of eddies of size r_0 in a turbulent flow with energy dissipation rate ε . From here on, we use “vorticity” and “rate of strain” both for the perceived as well as real quantities, the difference can be deduced from the scales given.

Here, we analyze the structure and the dynamics of \mathbf{M} , and its dependence on scale, thus extending our previous investigations¹⁴. Our experimental results at $R_\lambda = 350$ demonstrate that the dynamics of the alignment of vorticity with the eigenvectors of the rate of strain, measured at the time where the tetrahedron is regular, depends on r_0 through the rescaled time t/t_0 . This suggests the existence of a self-similar regime in the inertial range. At smaller Reynolds numbers, we found the dynamics to be scale dependent. The numerical results show that when $r_0 \rightarrow 0$ the properties of \mathbf{M} extrapolate smoothly to those of the true velocity gradient tensor, and the dynamics of alignment between vorticity and strain is qualitatively similar with one notable difference: the characteristic time scale for tetrahedra with size $r_0 \lesssim \eta$ is of the order of τ_K , the Kolmogorov time scale.

We begin, Section II, by describing the construction of the velocity gradient tensor \mathbf{M} . Our experimental and numerical techniques are explained in Section III. Section IV then presents our results concerning the evolution of the shape of the tetrahedra. In Section V, we discuss the instantaneous correlations between strain and vorticity at any instant, and their dependence on the scale r_0 . The dynamics of \mathbf{M} , in particular the alignment between vorticity and the initial eigenvectors of strain are presented in Section VI, which includes a subsection of simplified theoretical analysis of the alignment process at short times. Finally, Section VII contains our concluding remarks.

II. DEFINITION OF THE PERCEIVED VELOCITY GRADIENT TENSOR \mathbf{M}

Given fluid velocities at four points in a flow, we compute the perceived velocity gradient \mathbf{M} as follows^{13,14}. Denoting the positions of the four points as $\mathbf{x}^a(t)$, and their velocities as $\mathbf{u}^a(t)$, $a = 1, \dots, 4$, we express the positions and velocities with respect to the center of mass as $\mathbf{x}^a = \mathbf{x}^a - \mathbf{x}^0$, and $\mathbf{u}^a = \mathbf{u}^a - \mathbf{u}^0$, where $\mathbf{x}^0 = \frac{1}{4}(\mathbf{x}^1 + \mathbf{x}^2 + \mathbf{x}^3 + \mathbf{x}^4)$ and $\mathbf{u}^0 = \frac{1}{4}(\mathbf{u}^1 + \mathbf{u}^2 + \mathbf{u}^3 + \mathbf{u}^4)$. In full generality, M_{ij} is defined by minimizing the quantity:

$$K = \sum_{a=1}^4 \sum_{i=1}^3 \left(u_i^a - \sum_{j=1}^3 x_j^a M_{ji} \right)^2. \quad (1)$$

In the equation defining the quantity to be minimized, K , the indices a ($= 1, \dots, 4$) refer to the index of the point, and i, j ($= 1, \dots, 3$) to the component of the vector. By differentiating with respect to M_{ij} , one finds immediately that the condition to minimize K is:

$$\sum_{k=1}^3 g_{ik} M_{kj} = W_{ij}, \quad (2)$$

where the matrices \mathbf{g} and \mathbf{W} are defined by:

$$g_{ij} = \sum_{a=1}^4 x_i^a x_j^a \quad \text{and} \quad W_{ij} = \sum_{a=1}^4 x_i^a u_j^a. \quad (3)$$

Under the condition that \mathbf{g} is invertible, the matrix \mathbf{M} defined by:

$$\mathbf{M} = \mathbf{g}^{-1}\mathbf{W}, \quad (4)$$

provides the best fit approximation of \mathbf{M} based on four points.

As the flow is incompressible, we impose the constraint that $\text{tr}(\mathbf{M}) = 0$. This can be done by determining \mathbf{M} , as explained in the previous paragraph, and subtracting $\frac{1}{3}\text{tr}(\mathbf{M})\delta_{ij}$. Alternatively, returning to the minimization condition, Eq. (1), the trace can be imposed by adding a Lagrange multiplier, $\xi \sum_i M_{ii}$ to Eq. (1). The two definitions, although technically slightly different, lead to equal statistical properties, and to identical physical conclusions.

The construction used here, based on Eq. (4), explicitly requires the matrix \mathbf{g} to be invertible. As a symmetric matrix, \mathbf{g} is diagonalisable. Its eigenvalues g_i are positive, and $\sqrt{g_i}$ characterize the extent of the tetrahedra in the i^{th} eigendirection of \mathbf{g} . The matrix \mathbf{g} becomes non-invertible when one of its eigenvalue tends to zero. Thus, the condition that \mathbf{g} is invertible means physically that the four points of the tetrahedron are not coplanar. The technical difficulty associated with the minimization of the quantity K for highly flattened tetrahedra can be solved using standard Singular Value Decomposition algorithms²⁰.

In this work, we followed tetrahedra that are initially regular (close to regular in experiments), so as to identify flow properties at a single scale. The alignment dynamics studied here occurs *before* the tetrahedra become strongly deformed^{21,22} or we did not use the highly deformed tetrahedra in the analysis. As shown in Section IV the fraction of highly-flattened tetrahedra is negligible up to $t_0/4$ and only approximately 10% are highly-deformed at $t_0/2$. As will be shown in later chapters, the most interesting dynamics occur before $t_0/2$. To further reduce the effect of tetrahedron deformation on the accuracy of determination of \mathbf{M} , we excluded highly deformed tetrahedra from our statistics of \mathbf{M} (see details in Section IV). This comes at the cost that the number of samples in our statistics is slightly reduced.

Similar to the treatment of the true velocity gradient, it is convenient to decompose \mathbf{M} as the sum of a symmetric, strain-like part, \mathbf{S} , and an antisymmetric, vorticity-like part, $\mathbf{\Omega}$:

$$\mathbf{S} = \frac{1}{2}(\mathbf{M} + \mathbf{M}^T); \quad \mathbf{\Omega} = \frac{1}{2}(\mathbf{M} - \mathbf{M}^T). \quad (5)$$

The symmetric matrix \mathbf{S} describes the local straining motion. It is characterized by three real eigenvalues, λ_1 , λ_2 and λ_3 , associated with three eigenvectors \mathbf{e}_i . In the following, the three eigenvalues are sorted in decreasing order: $\lambda_1 \geq \lambda_2 \geq \lambda_3$. The antisymmetric matrix, $\mathbf{\Omega}$, describes the local rotation: $\Omega_{ij} = \frac{1}{2}\epsilon_{ijk}\omega_k$, where ϵ_{ijk} is the completely antisymmetric tensor, so that $\mathbf{\Omega} \cdot \mathbf{x} = \frac{1}{2}\boldsymbol{\omega} \times \mathbf{x}$. In the following, we characterize $\boldsymbol{\omega}$ by its norm $|\boldsymbol{\omega}|$ and its direction \mathbf{e}_ω , with $|\mathbf{e}_\omega| = 1$. In the limit of very small tetrahedra ($r_0 \ll \eta$), the tensor \mathbf{M} reduces to the true velocity gradient tensor \mathbf{m} , defined by $m_{ij} \equiv \partial_j u_i$, and the vector $\boldsymbol{\omega}$ defined above reduces to the usual definition of vorticity, $\boldsymbol{\omega} \equiv \nabla \times \mathbf{u}$.

III. EXPERIMENTS AND NUMERICAL SIMULATIONS

A. Experiments

Using image-based optical particle tracking, we measured experimentally the trajectories of tracer particles seeded in a swirling water flow between two counter-rotating baffled disks^{23,24}. Measurements were done in the center of the apparatus, where the residence time of particles is the largest. The maximum Taylor-microscale Reynolds number is $R_\lambda \approx 10^3$, where $R_\lambda \equiv \sqrt{15}u'^4/\nu\varepsilon$ with $u' \equiv \sqrt{\langle u_x^2 + u_y^2 + u_z^2 \rangle/3}$ being the fluctuation velocity and ν the kinematic viscosity. The symbol $\langle \rangle$ refers to the average of the fluctuating quantities in the flow. Measurements were carried out by using three high-speed CMOS cameras and high repetition rate frequency doubled Nd:YAG lasers. Our particle tracking algorithm²⁵ allowed us to follow simultaneously hundreds of particles in this intense turbulent flow. The measured trajectories, however, were frequently interrupted due to experimental artifacts such as the fluctuation of the illumination light intensity, the background and electronic noise. For multi-particle measurements, such as tetrahedra, it is very important to connect these interrupted trajectory segments in order to obtain better statistics at long-times. We therefore re-connected the trajectories in position-velocity space²⁶, which were then smoothed and differentiated to obtain instantaneous particle velocities²⁷.

In this paper, we focus on results from a measurement at $R_\lambda = 350$, at which the scale separation between the integral scale $L = u'^3/\varepsilon$ and the dissipative scale $\eta = (\nu^3/\varepsilon)^{1/4}$ is $L/\eta \approx 800$. As shown previously²⁸,

the temporal and spatial resolutions are sufficient to accurately measure the second moments of acceleration statistics.

From experimentally measured particle trajectories, we first identified instantaneous configurations of four points, separated from each other by a nominal distance r_0 , within a tolerance of $\pm 10\%$. Once identified, the trajectories of the tetrahedra were followed for as long as all four points remained in the field of view. Due to the limitation of particle seeding density in experiments, the data reported are mainly for tetrahedra with initial sizes between $L/17 - L/5$, or $50 - 180\eta$. In this range of scales, we followed $10^7 - 10^8$ tetrahedra. The small tolerance of inter-particle distances at the nominal values results in initially nearly isotropic tetrahedra²¹.

The particle trajectories used in this work were measured in an observation volume of size approximately $(2.5 \text{ cm})^3$ located at the center of the apparatus, where the flow has been documented to be very close to isotropic²⁴. Deviations from isotropy may be estimated from the well-known second order velocity structure functions, defined as $D_{LL}(\mathbf{r}) = \langle [(\mathbf{u}(\mathbf{x} + \mathbf{r}) - \mathbf{u}(\mathbf{x})) \cdot (\mathbf{r}/r)]^2 \rangle$ and $D_{NN}(\mathbf{r}) = \{ \langle [(\mathbf{u}(\mathbf{x} + \mathbf{r}) - \mathbf{u}(\mathbf{x}))]^2 \rangle - D_{LL} \} / 2$, where $r = |\mathbf{r}|$ is the separation distance. For isotropic turbulence, D_{LL} and D_{NN} depend only on r and they satisfy the following relations (see *e.g.*,²⁹): $D_{NN}(r)/D_{LL}(r) = 2$ for $r \ll \eta$ and $D_{NN}(r)/D_{LL}(r) = 4/3$. For the von Kármán flow in our experiment, due to the axisymmetric geometry, the statistics could depend on the angle θ between the axis of rotation and the separation vector \mathbf{r} . We found that for $40\eta \leq r \leq L/3$, the ratio $(3/4)D_{NN}(r, \theta)/D_{LL}(r, \theta)$ varies as a function of θ in the range $0.8 - 1.3$, but averages out to be very close to 1, the isotropic value, when considering all possible orientations of the separation. This provides evidence both that the dependence on the angle θ is weak, and that isotropy is recovered when averaging out over all possible directions^{30,31}. Further evidence that the anisotropies in our flow are not a concern comes from the fact that most experimental statistics derived from tetrahedra are in good agreement with DNS results using perfectly isotropic tetrahedra, see also¹⁴. The small deviation from precise isotropy in initial shapes, however, did give rise to discrepancies for certain quantities sensitive to initial shape, which we will discuss in detail later.

B. Direct Numerical Simulations

We used a spectral code to solve the Navier-Stokes equations for the (Eulerian) velocity field $\mathbf{u}(\mathbf{x}, t)$:

$$\partial_t \mathbf{u}(\mathbf{x}, t) + (\mathbf{u} \cdot \nabla) \mathbf{u}(\mathbf{x}, t) = -\nabla p(\mathbf{x}, t) + \nu \nabla^2 \mathbf{u}(\mathbf{x}, t) \quad (6)$$

$$\nabla \cdot \mathbf{u}(\mathbf{x}, t) = 0 \quad (7)$$

Eqs. (6) and (7) are integrated in a periodic box (size 2π), with up to 384^3 modes. Energy is injected into the flow at large scale by letting the low wavenumber modes $|k| \leq K$ (here, $K = 1.5$) evolve according to the Euler equations truncated to the shell $|k| \leq K$. This maintains a constant amount of energy at the largest scales³². Because the simulated flow is highly isotropic, we define the turbulence parameters based on the x component of velocity. The Reynolds number is

$$R_\lambda \equiv \frac{\lambda_g u'}{\nu}, \quad (8)$$

where the Taylor micro-scale defined as

$$\lambda_g^2 = \frac{u'^2}{\langle (\partial_x u_x)^2 \rangle}, \quad (9)$$

in which $u' \equiv \langle u_x^2 \rangle^{1/2}$. The Kolmogorov length scale is $\eta = (\nu^3/\varepsilon)^{1/4}$, where $\varepsilon = \nu \langle \partial_j u_i \partial_j u_i \rangle$. The available resolution has allowed us to simulate reliably turbulent flows up to a Reynolds number $R_\lambda = 170$. Quantitatively, the largest wavenumber faithfully simulated, k_{max} , is such that the product $k_{max} \times \eta \approx 1.4$.

Defining the integral length scale by $L = u'^3/\varepsilon$, the ratio L/η is approximately 300 at $R_\lambda = 170$. We note that L defined here is roughly twice as large as the correlation length scale of the Eulerian velocity field:

$$L_{corr} \equiv \frac{\pi}{2u'^2} \int_0^\infty k^{-1} E(k) dk \approx L/2, \quad (10)$$

where $E(k)$ is the energy spectrum.

With the Eulerian velocity field determined by solving numerically Eqs. (6) and (7), we also followed the motion of tetrahedra, whose vertices are tracer fluid particles, evolving according to:

$$\frac{d\mathbf{x}(t)}{dt} = \mathbf{u}(\mathbf{x}(t), t). \quad (11)$$

To this end, the values of \mathbf{u} , known after each time step on a regular grid of collocation points, are interpolated at the location $\mathbf{x}(t)$ of the Lagrangian tracers, using accurate third order schemes³³.

To study the dynamics using tetrahedra, we initialized tetrahedra of particles mutually separated by a distance r_0 , which we varied over the full range of available scales, $\eta \lesssim r_0 \lesssim L$. The statistical properties at a given scale r_0 have been determined by following at the minimum 125,000 tetrahedra.

IV. DEFORMATION OF THE TETRAHEDRA

We consider here the deformation occurring over a short time scale, while the process of alignment between the perceived vorticity and strain is taking place. To quantify the deformation of tetrahedra, it is convenient to introduce the tensor \mathbf{g} , defined in Eq. (3), and its eigenvalues^{14,21,22,34,35}. The trace of \mathbf{g} , which is the square of the radius of gyration of the four points, quantifies the overall size of the object. The tensor $\mathbf{I} \equiv \mathbf{g}/\text{tr}(\mathbf{g})$, whose trace is 1, characterizes the shape of the object. Specifically, because \mathbf{I} is a symmetric matrix, it can be diagonalized in an orthogonal basis formed by its eigenvectors \mathbf{e}_{I_i} . In the following, we arrange the eigenvalues of \mathbf{I} in decreasing order: $I_1 \geq I_2 \geq I_3$. Since $I_1 + I_2 + I_3 = 1$, a regular tetrahedron corresponds to $I_1 = I_2 = I_3 = 1/3$, while a nearly co-planar configuration gives $I_3 \approx 0$.

The matrix \mathbf{g} is related to the moment of inertia tensor, \mathbf{J} , familiar in the context of mechanics of solid bodies, by¹⁴:

$$J_{ij} \equiv \text{tr}(\mathbf{g})\delta_{ij} - g_{ij}. \quad (12)$$

A. Alignment of tetrahedron geometry with the eigenvectors of the rate of strain

The dynamics of tetrahedra is strongly influenced by the local rate of strain. In particular, it has been demonstrated¹⁴ that the stretching in the direction of the largest eigenvalue of the strain, \mathbf{e}_1 , leads to an elongation of the tetrahedron in this direction, and, by conservation of angular momentum, to an alignment of the vorticity $\omega(t)$ in the direction $\mathbf{e}_1(0)$. The results presented here generalize this observation: at short times, the deformation of the tetrahedra is very well aligned with the eigendirection of the eigenvectors of the rate of strain tensor.

Fig. 1 shows how the principal axes of initially regular tetrahedra, $\mathbf{e}_{I_i}(t)$, align with the eigenvectors of the rate of strain, $\mathbf{e}_i(0)$. For initially isotropic tetrahedra, as in DNS, the matrix \mathbf{I} is diagonal at $t = 0$. A very small deformation of the tetrahedra due to the strain breaks the isotropy, and leads to the immediate alignment of the principal axes of the tetrahedra with the strain eigenvectors. This is reflected in Fig. 1 by the perfect alignment between $\mathbf{e}_k(0)$ and $\mathbf{e}_{I_k}(t)$ at very small times t ($t = 0^+$). By $t = 0^+$, we refer to a strictly positive, but very small value of time. The tetrahedra studied experimentally are not exactly isotropic initially. Instead, the eigenvalues of \mathbf{I} are slightly different from each other: $I_i = \frac{1}{3} + \delta I_i$, where $|\delta I_i| \ll 1$. At $t = 0$, the corresponding three eigenvectors of \mathbf{I} are uncorrelated with the strain eigenvectors, i.e., $\langle [\mathbf{e}_{I_k}(0) \cdot \mathbf{e}_j(0)]^2 \rangle \approx 1/3$. This explains the difference at short times seen in Fig. 1 between the curves obtained from DNS and from experiment. On the other hand, under the action of the strain, the tetrahedra deform quickly and their principal axes align with the eigenvectors of the strain in a time of approximately $t_0/10$, after which the tetrahedron evolution is independent of initial shape. We note that over the range of scales shown here, $L/16 \leq r_0 \leq L/2$, the dynamics of alignment is essentially self-similar, once expressed in units of t_0 . In a time of order t_0 , the axes $\mathbf{e}_{I_k}(t)$ lose any memory of the initial alignment with $\mathbf{e}_j(0)$; all values of $\langle [\mathbf{e}_{I_k}(t) \cdot \mathbf{e}_j(0)]^2 \rangle$ relax towards $1/3$. This is consistent with the fact that t_0 , which is the time introduced in Kolmogorov theory, is the proper correlation times of an object initially with a scale r_0 . Small deviations are visible for DNS data of $r_0 = L/16 \approx 20\eta$, which is known to be the lower limit of the inertial range.

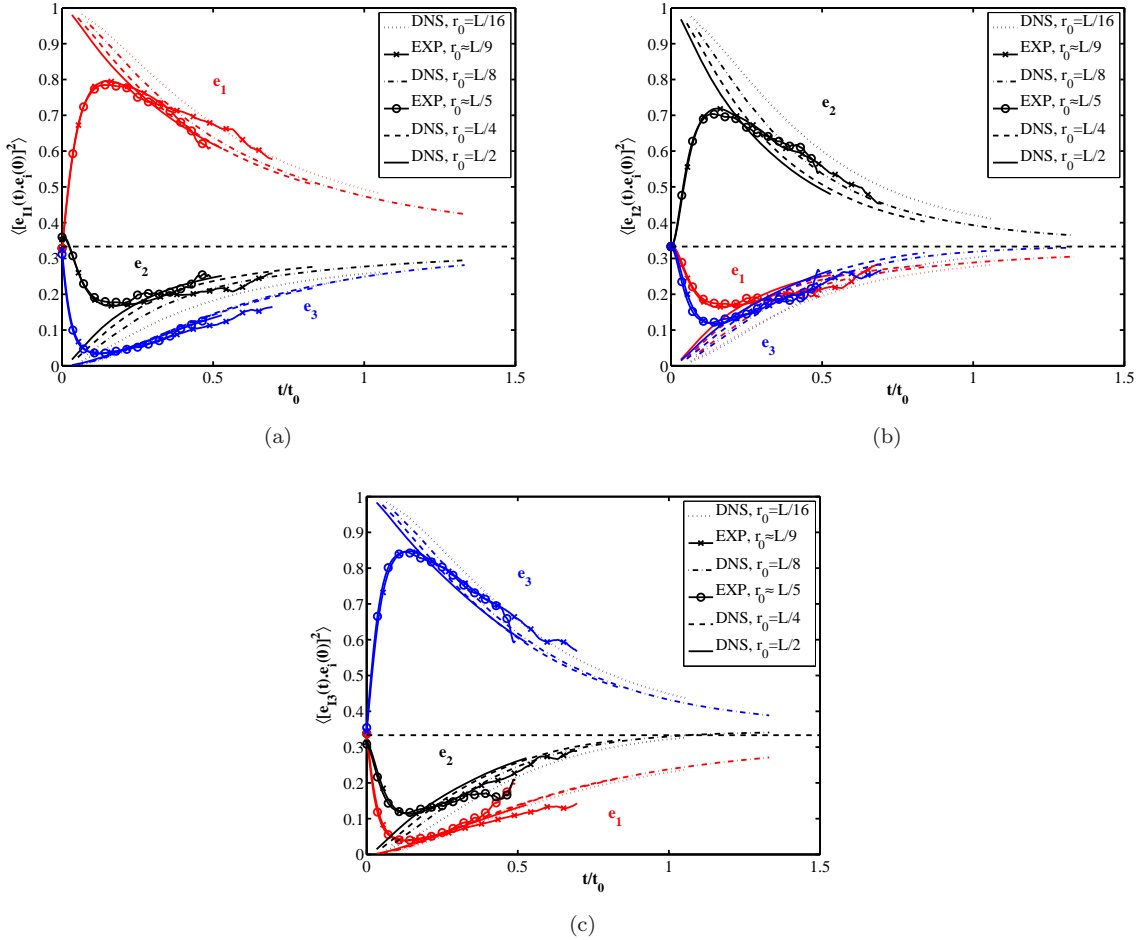


FIG. 1. (Color online) Deformation of tetrahedra: alignment of the principal axes of the tetrahedra with the eigenvectors of the strain. The ensemble averages $\langle [e_{Ii}(t) \cdot e_j(0)]^2 \rangle$ as a function of time for (a) $i = 1$ (longest axis), (b) $i = 2$ (intermediate axis) and (c) $i = 3$ (shortest axis of the tetrahedron). As expected, the i^{th} axis of the tetrahedron, $e_{Ii}(t)$, aligns perfectly at very short times with the i^{th} eigenvector of the strain, $e_i(0)$. After a time of order $\sim t_0$, the alignment relaxes and the axes of the tetrahedron do not show any particular alignment with any of the eigenvectors of the strain. The DNS data correspond to $R_\lambda = 170$, whereas the experiments to $R_\lambda = 350$.

B. Flattening of the tetrahedra

Along with the stretching of the tetrahedra in the direction $e_1(0)$, documented in particular in¹⁴, one expects a strong compression in the direction $e_3(0)$, corresponding to the most negative eigenvalue of the perceived strain. This has been shown to lead to very significantly flattened tetrads^{21,22,35}. In particular, the probability distribution function (PDF) of I_3 is sharply peaked around 0 at late times, $t/t_0 \gtrsim 1$. As explained in Section II, this can be the cause of a serious limitation in our construction of the perceived velocity gradient, as implied by Eq. (4). A good understanding of the dynamics leading to flattened tetrahedra is thus of interest not only for its own sake, but also in relation to the dynamics of alignment between perceived vorticity and strain. This subsection therefore discusses the flattening of tetrahedra, and demonstrates that the formation of very flat configurations is not faster than the alignment process between vorticity and strain.

To this end, Fig. 2 shows the evolution of the PDF of I_3 (a), and the evolution of the probability that the value of I_3 is less than a very small number, $I_3 \leq 10^{-3}$ (b). Initially, the probability of I_3 is peaked near $I_3 = 1/3$. In DNS, which starts with precisely isotropic tetrahedra, the PDF is originally a δ -function at $I_3 = 1/3$. In experiments, where we select particles that form nearly isotropic tetrahedra, the initial PDF

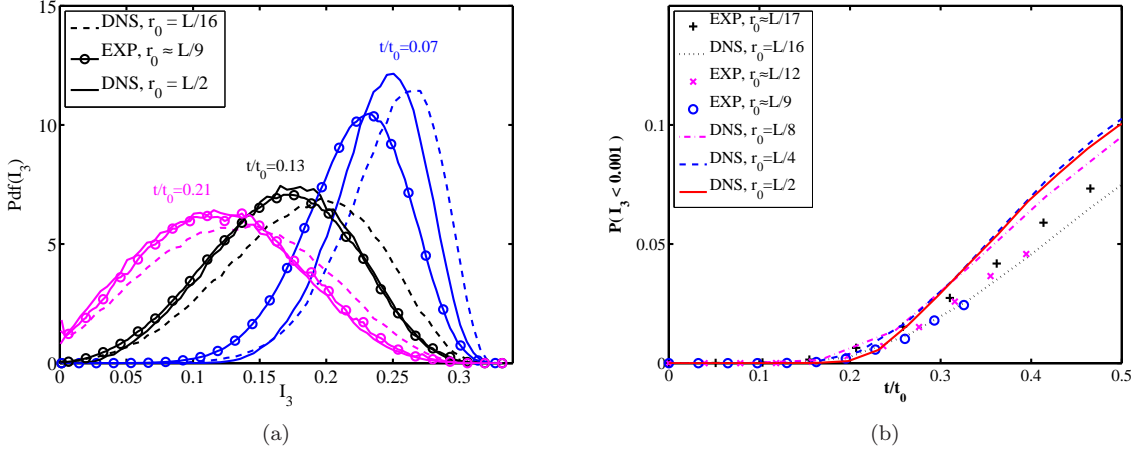


FIG. 2. (Color online) Flattening of tetrahedra. (a) PDF of I_3 at several times, $t/t_0 = 0.07$, 0.13 and 0.21 , for different initial tetrahedron sizes (r_0 from $L/16$ to $L/2$) in both DNS ($R_\lambda = 170$) and experiment ($R_\lambda = 350$). The observed peak of the PDF decreases when time increases. At $t = 0.21t_0$, a non-zero PDF at $I_3 \approx 0$ is observed. The probability that $I_3 \leq 10^{-3}$ is shown in (b) for several values of r_0 , as a function of the normalized time t/t_0 . A steep growth of the probability $P(I_3 \leq 10^{-3})$ is seen for $t \gtrsim t_0/4$. The growth of the probability does not depend much on the scale r_0 over the inertial range: from $r_0 = L/16 \approx 20\eta$ in DNS and $r_0 = L/17 \approx 50\eta$ in experiments to $r_0 = L/2$.

is not a δ -function, but is still narrowly distributed around $I_3 \approx 0.3$, as shown before²¹. As time increases, the peak of the PDF shifts towards smaller values of I_3 (Fig. 2a), reflecting a tendency of the tetrahedra to flatten. The evolution of the PDF does not depend very much on the initial size of the tetrahedron, as seen when comparing DNS and experimental data ranging from $r_0 = L/16 \approx 20\eta$ in DNS to $r_0 = L/2$. A noticeable fraction of the tetrahedra becomes flattened after $t \gtrsim t_0/4$ (see Fig. 2(b)), consistent with the sharply peaked distribution of I_3 observed at later times^{21,22,35}. From a flat configuration, with all points in the same plane, it is not possible to extract any information on the variation of the velocity in the plane transverse to the plane. As explained in Section II however, this does not prevent us from computing \mathbf{M} using Singular Value Decomposition. However, it points to a limitation on the accuracy of the procedure. Therefore, in the results reported here, we excluded tetrahedra with $I_3 \leq 10^{-3}$ from the statistics of \mathbf{M} . As seen from Fig. 2(b), this leads to at maximum a 10% reduction in the number of samples at time $t/t_0 = 0.5$, while most of the interesting dynamics occurs before this time.

The results of this section thus show a very strong alignment between the axes of the tetrahedra and those of strain, see Fig. 1, and that the dynamics of flattening of the tetrahedra happens over a time of the order of $t_0/4$, see Fig. 2. In addition, we find that the dynamics is essentially self-similar, insofar as the time-dependent correlations presented here are independent of scale, once time has been expressed in units of t_0 . This is consistent with earlier results²¹ demonstrating that the evolution of the shape factors, $I_i(t)$, is also self-similar. The ensuing picture is thus that in a statistical sense, initially regular tetrahedra of size r_0 evolves with a time scale $\sim (r_0^2/\varepsilon)^{1/3}$, when r_0 in the inertial range.

V. PROPERTIES OF \mathbf{M} : SCALE DEPENDENCE (INSTANTANEOUS STATISTICS)

Previous investigations^{6,10,16,17,36} of the structure of the true velocity gradient tensor, \mathbf{m} , reveal two main properties of the instantaneous statistics of \mathbf{m} :

(i) The direction of the vorticity \mathbf{e}_ω is preferentially aligned with \mathbf{e}_2 , the direction of the intermediate eigenvalue of the rate of strain, $\mathbf{s} = \frac{1}{2}(\mathbf{m} + \mathbf{m}^T)$, but does not show any particular alignment with \mathbf{e}_1 , the strongest eigen-direction of the rate of strain.

(ii) The intermediate eigenvalue of the rate of strain, λ_2 , is mostly positive, which implies that the product of the eigenvalues of \mathbf{s} is negative and thus ensures vortex stretching $\langle \boldsymbol{\omega} \cdot \mathbf{s} \cdot \boldsymbol{\omega} \rangle \geq 0$, an important property of turbulent flows³⁷.

It is natural to ask what are the instantaneous properties of the perceived velocity gradient \mathbf{M} .

On general grounds, one expects that the properties of \mathbf{M} will depend on the size r_0 . For $r_0 \lesssim \eta$, \mathbf{M} coincides with the true velocity gradient tensor. As the separation r_0 between the points of the tetrahedron increase, the velocities at the four points become less and less correlated. For $r_0 \gg L$, \mathbf{M} is not expected to reflect any particular property of the turbulent dynamics. On the other hand, one may expect that in the inertial range, some properties become scale-independent, consistent with the notion that the flow shows some degree of self-similarity.

A. Alignment between vorticity and strain

The PDFs of the cosines of the instantaneous angles between \mathbf{e}_ω and \mathbf{e}_i , are shown in Fig. 3. The PDF for $i = 1$ (Fig. 3(a) and (b)) hardly varies through scale, and remains nearly uniform: $P(|\mathbf{e}_1 \cdot \mathbf{e}_\omega|) \approx 1$, consistent with previous observations with the true velocity gradient tensor^{6,17}. In Fig. 3(c) and (e), the alignment corresponding to the true velocity gradient tensor \mathbf{m} (*i.e.*, $r_0 = 0$) are the ones with the largest variations. As scale increases, the alignment between \mathbf{e}_2 and \mathbf{e}_ω becomes less pronounced, as shown by the observed decrease of the PDF at $|\mathbf{e}_2 \cdot \mathbf{e}_\omega| = 1$. Similarly, the tendency of \mathbf{e}_ω to be perpendicular to \mathbf{e}_3 diminishes when scale increases. As the scale r_0 approaches L , the PDF becomes flat. This tendency can be clearly seen in Fig. 4, which shows the averaged values $\langle (\mathbf{e}_i \cdot \mathbf{e}_\omega)^2 \rangle$. When r_0 increases from dissipative to integral scales, $\langle (\mathbf{e}_\omega \cdot \mathbf{e}_2)^2 \rangle$ continuously decreases from the larger magnitude for the true velocity gradient tensor (shown by the horizontal dashed lines in Fig. 4) towards $1/3$, which corresponds to two randomly selected vectors. In the same spirit, $\langle (\mathbf{e}_\omega \cdot \mathbf{e}_3)^2 \rangle$ continuously increases from the lower magnitude of the velocity gradient tensor to $1/3$ when r_0 increases. In Fig. 4 are shown both the numerical data ($R_\lambda = 170$, open symbols) and the experimental data ($R_\lambda = 350$, filled symbols). Remarkably, in both Figs. 3 and 4, the lower Reynolds number data show a continuous variation of the statistics of the cosines $\mathbf{e}_2 \cdot \mathbf{e}_\omega$ and $\mathbf{e}_3 \cdot \mathbf{e}_\omega$ with scale. The variation is particular strong when r_0 decreases towards the dissipative range, *i.e.*, for $r_0 \lesssim L/16 \approx 20\eta$. In comparison, the higher Reynolds number data suggest that over the accessible range of scales, the properties of the flow are essentially scale independent. This suggests that at sufficiently large Reynolds numbers, the dynamics of \mathbf{M} may show some self-similarity, as far as the relation between vorticity and strain is concerned. This remains to be studied further with data at larger Reynolds numbers.

The results summarized in Figs. 3 and 4 thus show that the alignment properties of \mathbf{e}_ω and \mathbf{e}_2 , or the orthogonality between \mathbf{e}_ω and \mathbf{e}_3 , are observable throughout the entire inertial range. This is to be contrasted with the lack of alignment between \mathbf{e}_ω and \mathbf{e}_1 , which is observed over all the scales that we have studied.

B. The intermediate eigenvalues of the rate of strain

We now turn to the statistics of λ_i , the eigenvalues of the rate of strain. Whereas it is clear, from the relations $\lambda_1 \geq \lambda_2 \geq \lambda_3$ and $\lambda_1 + \lambda_2 + \lambda_3 = 0$ that $\lambda_1 \geq 0$ and $\lambda_3 \leq 0$, the sign of λ_2 can be either positive or negative. To quantify the relative value of λ_2 compared to λ_1 and λ_3 , it is convenient to introduce the dimensionless variable β , defined by¹⁷:

$$\beta \equiv \frac{\sqrt{6} \lambda_2}{\sqrt{\lambda_1^2 + \lambda_2^2 + \lambda_3^2}}. \quad (13)$$

This definition ensures that $-1 \leq \beta \leq 1$.

The PDF of β is shown in Fig. 5a for several values of r_0 . At small Reynolds number, the PDFs show a clear evolution as a function of the scale r_0 . In the dissipative range ($r_0 = 0$, *i.e.*, for the true velocity gradient tensor), a strong bias towards high values of β is observed. As r_0 increases, the PDFs show a reduced bias towards high values of β . For the highest Reynolds number experimental flow, the PDF of β changes little throughout the limited range of measured scales. As shown in Fig. 5b, the mean $\langle \beta \rangle$ remains positive throughout the entire inertial range, dropping from $\langle \beta \rangle \approx 0.285$ for $r_0 = 0$, to $\langle \beta \rangle \approx 0.07$ for $r_0 \approx L$ for the low Reynolds number data. On the contrary, the value for the higher Reynolds number experimental flow, in the range $1/17 \leq r_0/L \leq 1/5$ is close to 0.13. Figure 5 suggests that the dependence of $\langle \beta \rangle$ on scale is relatively weak in the inertial range $L/16 \lesssim r_0 \lesssim L/2$, in particular at the highest Reynolds number. This is consistent with the trend observed in subsection V A, which points to a scale-independent structure of \mathbf{M} in the inertial range at sufficiently high Reynolds numbers.

The results of this section suggest a smooth change of the structure of \mathbf{M} throughout the range of scales. Whereas no particular alignment between \mathbf{e}_ω and \mathbf{e}_1 is observed, irrespective of the size of the tetrahedron,

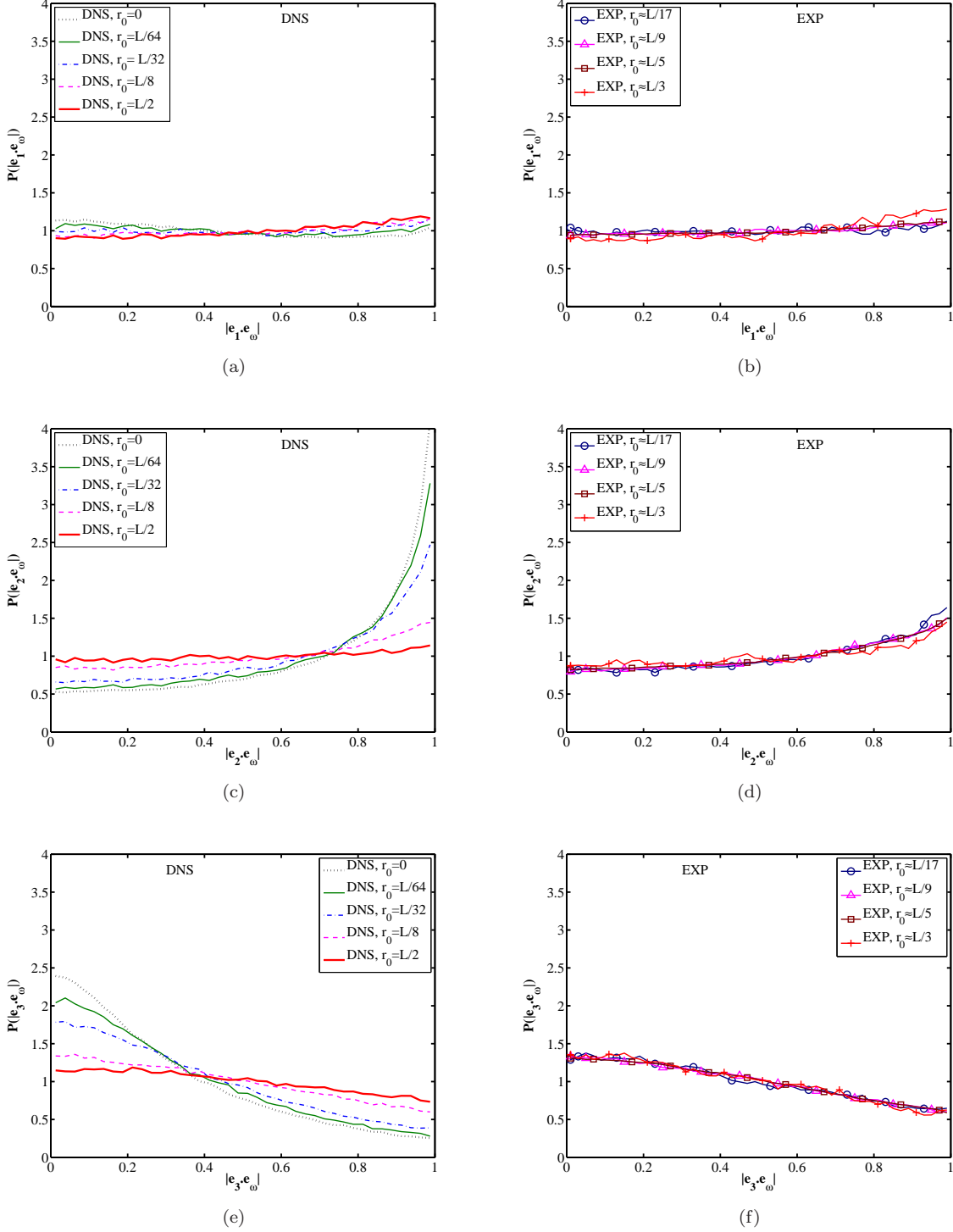


FIG. 3. (Color online) Scale dependence of the alignment of vorticity and strain (instantaneous statistics): The PDFs of $|\mathbf{e}_i \cdot \mathbf{e}_\omega|$ from both DNS (panels a,c,e) and experiments (panels b,d,f) for tetrahedra with different sizes r_0 from dissipative ($r_0 = 0$ in DNS) to integral ($L/2$) scales. Panels (a) and (b) are for $i = 1$; (c) and (d) for $i = 2$; and (e) and (f) for $i = 3$. The lack of alignment of vorticity with \mathbf{e}_1 is nearly independent of scale. The PDF of $|\mathbf{e}_\omega \cdot \mathbf{e}_2|$ sharply peaks at 1 at very small scales, in particular for the true velocity gradient tensor ($r_0 = 0$). The effect weakens as the scale increases. Similarly, the maximum at 0 of the PDF of $|\mathbf{e}_\omega \cdot \mathbf{e}_3|$ at very small scales becomes milder as scale increases. The DNS data correspond to $R_\lambda = 170$, whereas the experiments to $R_\lambda = 350$.

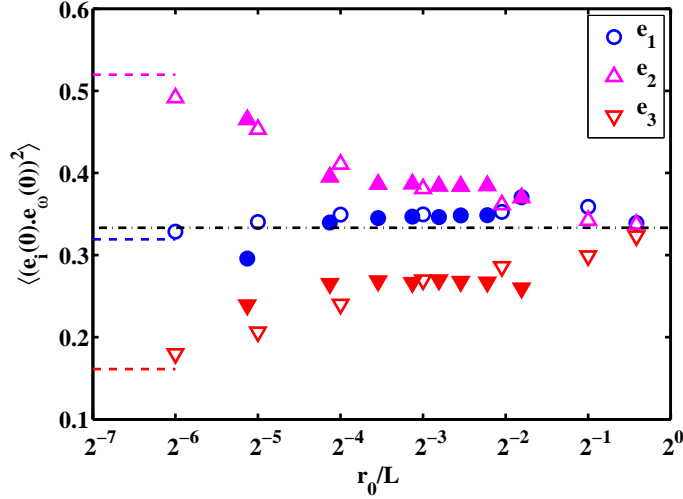


FIG. 4. (Color online) The mean values $\langle (\mathbf{e}_i(0) \cdot \mathbf{e}_\omega(0))^2 \rangle$. The open symbols are DNS data ($R_\lambda = 170$) and the filled symbols are experimental results ($R_\lambda = 350$).

the tendency of \mathbf{e}_ω to align with \mathbf{e}_2 (respectively to be perpendicular to \mathbf{e}_3) is the strongest for $r_0 \rightarrow 0$, *i.e.*, for the true velocity gradient tensor \mathbf{m} , and decreases for \mathbf{M} with increasing r_0 . Similarly, the intermediate eigenvalue of the rate of strain is comparatively more positive for the true velocity gradient tensor \mathbf{m} than for \mathbf{M} at values of r_0 in the inertial range. As the scale r_0 increases towards the inertial length L , the PDF of β becomes more symmetric about $\beta = 0$, as expected from a random matrix.

Thus, the perceived velocity gradient tensor \mathbf{M} in the inertial range shares many essential properties with the true velocity gradient tensor \mathbf{m} . Our observations thus suggest a continuity in the behavior from the dissipative to the inertial range. Remarkably, the data obtained with the higher Reynolds number experimental flow suggest that the structural properties of \mathbf{M} become scale independent in the inertial scale. This should be confirmed by studying flows at even higher Reynolds numbers.

VI. PROPERTIES OF M: DYNAMICS (TEMPORAL CORRELATIONS)

The main observation in our recent study¹⁴ was the dynamical alignment of vorticity with the leading eigenvector of the rate of strain, which we were able to study conveniently by investigating the correlation between $\mathbf{e}_1(0)$ and $\mathbf{e}_\omega(t)$, *i.e.*, with a time delay. Hence the lack of alignment between $\mathbf{e}_\omega(t)$ and $\mathbf{e}_1(t)$ (Figs. 3(a) and (b)) is a consequence of the de-correlation of the vector \mathbf{e}_1 itself in a time t , which counteracts the alignment of $\mathbf{e}_\omega(t)$ with $\mathbf{e}_1(0)$.

A consequence of the previous section is that it is not *a priori* clear that the alignment of $\mathbf{e}_\omega(t)$ with $\mathbf{e}_i(0)$ ($i = 2$ or $i = 3$) is going to be self-similar, *i.e.*, that the angle between $\mathbf{e}_\omega(t)$ and $\mathbf{e}_i(0)$ ($i = 2$ or $i = 3$) is going to depend only on t/t_0 , as it had been found for the angle between $\mathbf{e}_\omega(t)$ and $\mathbf{e}_1(0)$ ¹⁴. This is due to the fact that the PDFs of $|\mathbf{e}_\omega(0) \cdot \mathbf{e}_i(0)|$, for $i = 2$ and $i = 3$ change with the scale r_0 for small scale separation L/η .

A. Averaged alignment of the direction of vorticity with the eigenvectors of the rate of strain

Fig. 6(a) shows that, as time increases, the vector $\mathbf{e}_\omega(t)$ tends to become better aligned with $\mathbf{e}_1(0)$. As reported previously¹⁴, the statistics characterizing the alignment of the two vectors is essentially independent of the scale r_0 , once time t is rescaled by t_0 . The characteristic time scale for this process, Fig. 6(a) is of order $t_0/5$. For the DNS at $R_\lambda = 170$, the alignment of $\mathbf{e}_\omega(t)$ with $\mathbf{e}_2(0)$, and to a lesser extent with $\mathbf{e}_3(0)$, shows a significant dependence on scale, see Fig. 6(b) and (c). Note that for $t = 0$, the difference was shown as a function of r_0/L in Fig. 4. In comparison, the experimental data obtained at $R_\lambda = 350$ shows a much reduced variation as a function of scale (see also Fig. 4). We also notice that $\langle [\mathbf{e}_2(0) \cdot \mathbf{e}_\omega(t)]^2 \rangle$ is almost

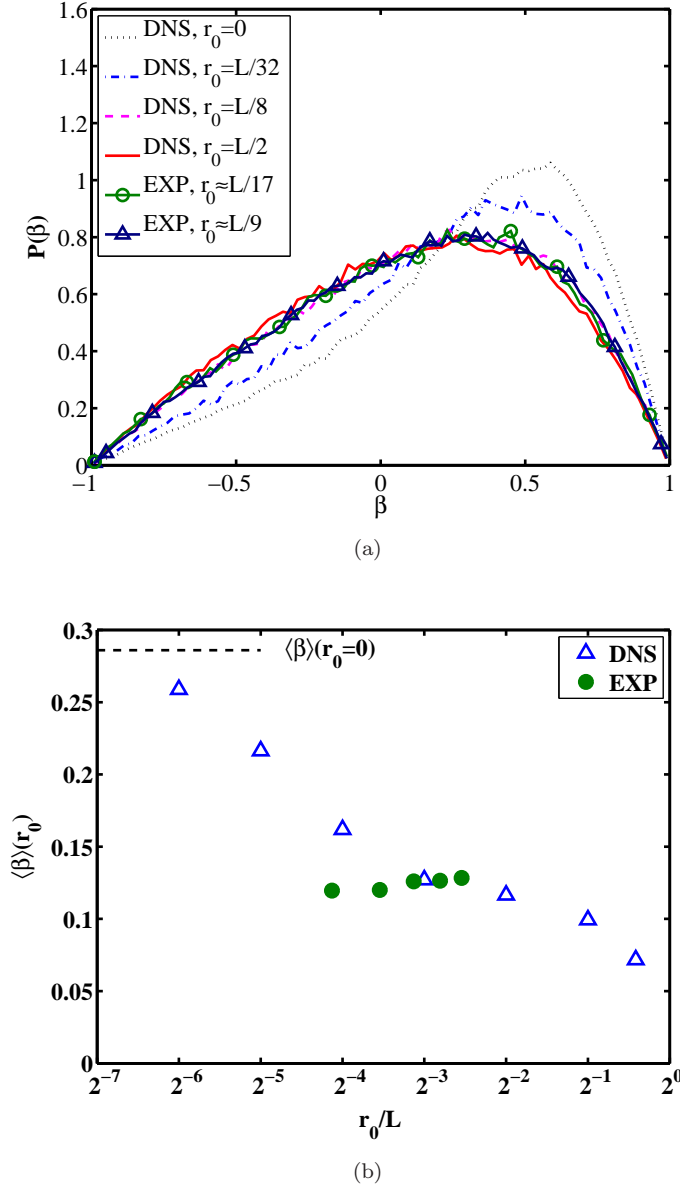


FIG. 5. (Color online) Dependence of the intermediate eigenvalue of strain on scale r_0 . (a) PDF of β , as defined in Eq. 13, for several values of r_0 . (b) The average value of β as a function of scale, in which the dashed line indicates $\langle \beta \rangle$ for the true velocity gradient \mathbf{m} as $r_0 \rightarrow 0$. The DNS data correspond to $R_\lambda = 170$, whereas the experiments to $R_\lambda = 350$.

constant, *i.e.*, the slope at $t = 0$ is much smaller than the slopes for $\mathbf{e}_1(0)$ and $\mathbf{e}_3(0)$. These features can be understood by the elementary considerations presented in subsection VI B.

We note that the time scale of the alignment of $\mathbf{e}_\omega(t)$ with $\mathbf{e}_1(0)$ and $\mathbf{e}_3(0)$ are comparable to the time scale characterizing the deformation of the tetrahedra (see Section IV). This is a strong indication that the deformation is an important part of the dynamical process, see also^{14,38}. A theoretical description of the dynamics of \mathbf{M} has therefore to take into account in an essential way the deformation of the tetrahedra¹³.

Not only the mean values of $[\mathbf{e}_1(0) \cdot \mathbf{e}_\omega(t)]^2$ evolve as a function of t/t_0 in a self-similar way, but also the PDFs of $|\mathbf{e}_1(0) \cdot \mathbf{e}_\omega(t)|$ (see Figures 7(a), (d), and (g)). This situation is to be contrasted with the evolution of the alignment between $\mathbf{e}_\omega(t)$ and $\mathbf{e}_2(0)$ or $\mathbf{e}_3(0)$. Figures 7(b), (e), and (h) show that the PDF of the angle between $\mathbf{e}_2(0)$ and $\mathbf{e}_\omega(t)$ is essentially independent of t/t_0 for $0 \leq t/t_0 \leq 0.2$, consistent with Fig. 6(b). The

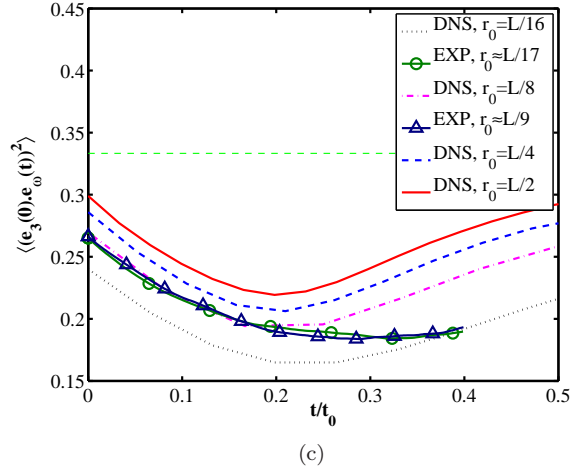
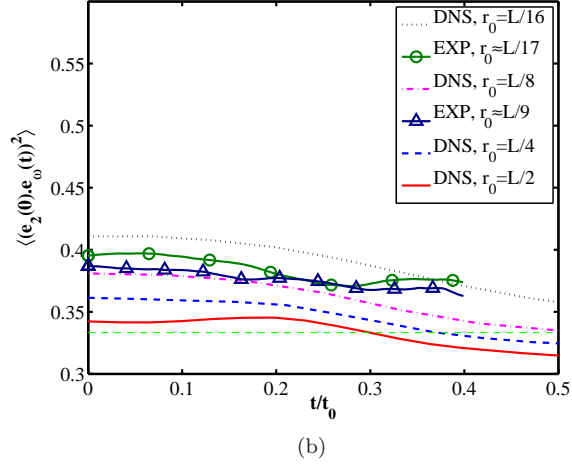
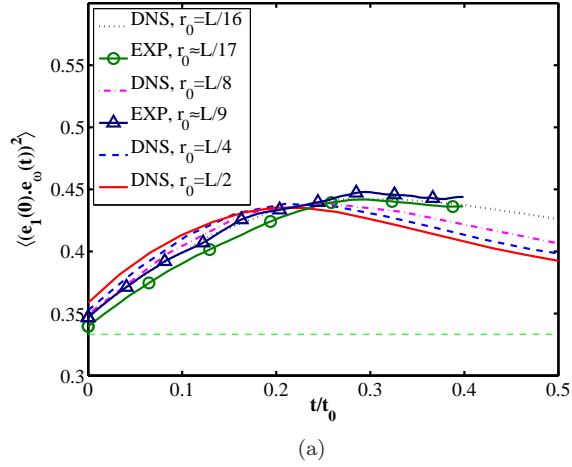


FIG. 6. (Color online) Alignment between $\mathbf{e}_\omega(t)$ and $\mathbf{e}_i(0)$. Ensemble averages $\langle [\mathbf{e}_i(0) \cdot \mathbf{e}_\omega(t)]^2 \rangle$ for $i = 1$ (a), $i = 2$ (b) and $i = 3$ (c) as a function of the time delay t , normalized by t_0 . The initial tetrahedron size, r_0 , are all in the inertial range. The evolution of the alignment of $\mathbf{e}_\omega(t)$ with $\mathbf{e}_1(0)$ suggests a self-similarity: The curves in (a) all superpose once t is expressed in units of t_0 . The alignment of $\mathbf{e}_\omega(t)$ with $\mathbf{e}_2(0)$ and $\mathbf{e}_3(0)$ shows a stronger dependence on r_0 , consistent with the scale dependence of the *instantaneous* alignment properties of \mathbf{e}_ω with \mathbf{e}_2 and \mathbf{e}_3 (Fig. 3). The DNS data correspond to $R_\lambda = 170$, whereas the experiments to $R_\lambda = 350$.

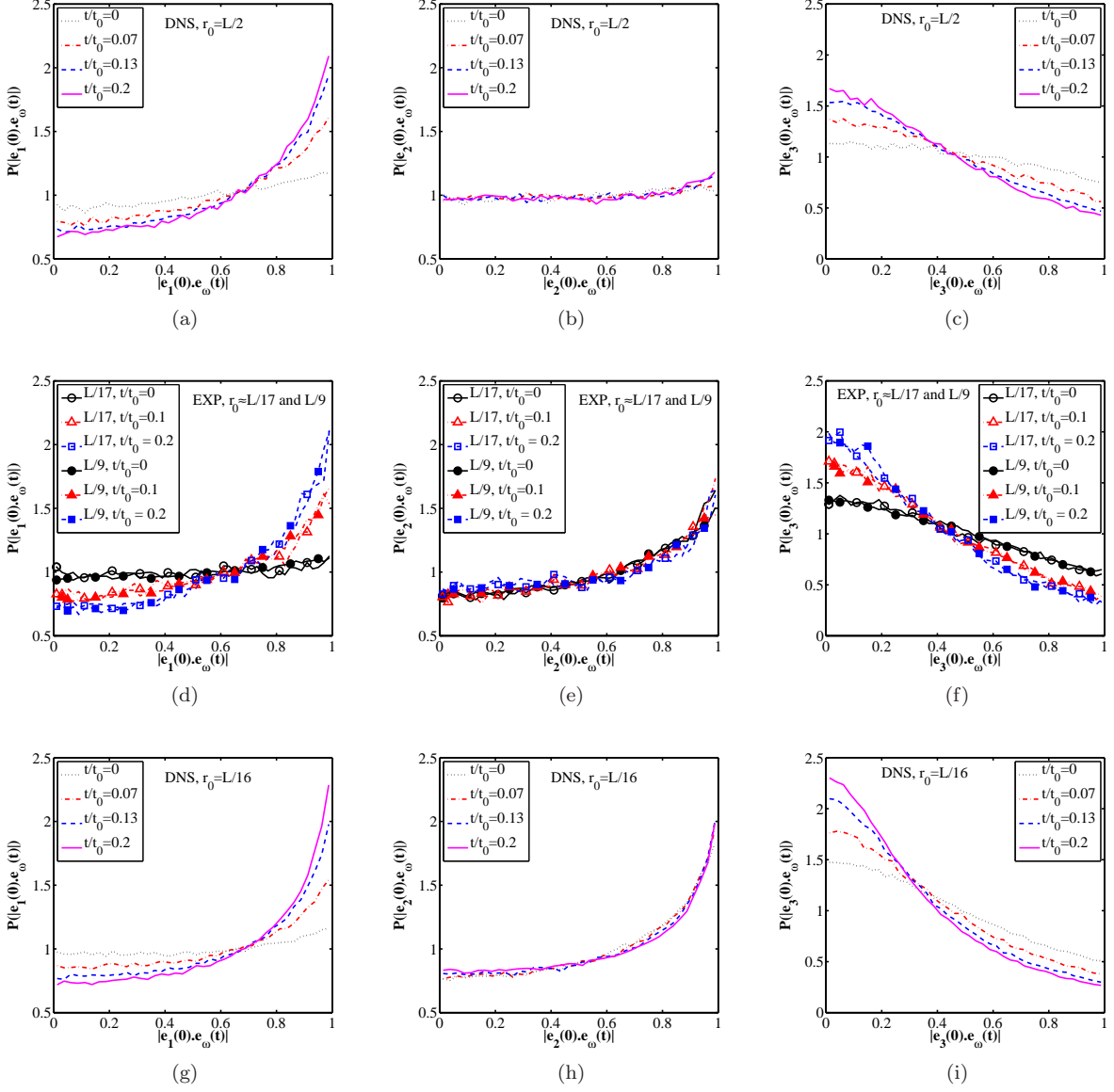


FIG. 7. (Color online) Evolution of the angle between $\mathbf{e}_i(0)$ and $\mathbf{e}_\omega(t)$. The PDF of $|\mathbf{e}_i(0) \cdot \mathbf{e}_\omega(t)|$ is shown for times between $0 \leq t/t_0 \leq 0.2$, and at three values of r_0 : $r_0 = L/2$ in DNS ($R_\lambda = 170$) (a)-(c), $r_0 \approx L/9$ and $r_0 \approx L/17$ in experiment ($R_\lambda = 350$) (d)-(f), and $r_0 = L/16$ in DNS (g)-(i). Panels (a), (d) and (g) are for $i = 1$. Consistent with previous results¹⁴, the evolution of these PDFs is essentially self-similar for r_0 in the inertial range. Panels (b), (e) and (h) are for $i = 2$. The PDFs hardly change over the range of times shown; however, they depend significantly on the value of r_0 . Panels (c), (f) and (i) are for $i = 3$. During the period of time shown, the PDFs evolve to peak at 0, *i.e.*, $\mathbf{e}_\omega(t)$ tends to become perpendicular to $\mathbf{e}_3(0)$. There is also a moderate dependence on scale r_0 .

direction $\mathbf{e}_\omega(t)$ is strongly aligned with $\mathbf{e}_2(0)$ at small values of r_0 , much less so as the value of r_0 increases towards L . Last, as shown in Figs. 7(c), (f), and (i), $\mathbf{e}_\omega(t)$ becomes more perpendicular to $\mathbf{e}_3(0)$ within $t/t_0 \lesssim 0.2$ and the tendency is stronger at small values of r_0 .

In summary, the main observation of this subsection is that, contrary to the alignment of $\mathbf{e}_\omega(t)$ with $\mathbf{e}_1(0)$, which evolves in an essentially self-similar manner, the dynamics of the alignment of $\mathbf{e}_\omega(t)$ with $\mathbf{e}_2(0)$ and $\mathbf{e}_3(0)$ proceeds in a way that depends on the size of the tetrahedra, at least for our Reynolds numbers, a result that was expected in view of the observation that the average values of $(\mathbf{e}_i(0) \cdot \mathbf{e}_\omega(0))^2$ show a clear dependence on scale.

B. Elementary modeling considerations

The analysis presented below, which aims only at capturing some of the main features of the alignment process, rests on several important assumptions. We restrict ourselves here to very short time scales, which effectively allows us to neglect the coupling between shape and vorticity. We are merely investigating here the evolution of vorticity, at the lowest order in terms of a Taylor-series expansion. Effectively, coupling terms between shape and vorticity, as well as feedback between vorticity and strain all would be seen only at higher order, independently of the form of the model. The limitation of this approach is that it does not allow us to properly describe the coupling between shape deformation and the evolution of vorticity. To describe the evolution of \mathbf{M} , models based on the Restricted Euler approximation^{39–41} and its subsequent elaborations, reviewed in¹⁸, have been used very often. The resulting equation for the evolution of the vorticity is:

$$\frac{d\omega_i}{dt} - S_{ij}\omega_j = 0. \quad (14)$$

which can also be obtained directly from the Euler equation. A full description of \mathbf{M} requires also an equation for the evolution of the rate of strain, \mathbf{S} , which involves the second derivatives of pressure (pressure hessian), a quantity notoriously difficult to model. While it may be possible to extract information concerning the strain evolution from the available data, we restrict ourselves here to the evolution of vorticity, and focus exclusively on Eq. 14.

An evolution equation for the direction of vorticity \mathbf{e}_ω can be readily obtained by taking the double vector product of Eq. 14 with \mathbf{e}_ω , which immediately leads to:

$$\frac{d\mathbf{e}_\omega}{dt} = \mathbf{S} \cdot \mathbf{e}_\omega - (\mathbf{e}_\omega \cdot [\mathbf{S} \cdot \mathbf{e}_\omega])\mathbf{e}_\omega \quad (15)$$

To proceed, we project \mathbf{e}_ω on the three eigenvectors of \mathbf{S} :

$$\mathbf{e}_\omega = \sum_{i=1}^3 c_i \times \mathbf{e}_i \quad (16)$$

The constraint $|\mathbf{e}_\omega|^2 = 1$ implies that $\sum_{i=1}^3 c_i^2 = 1$. Eq. 15 can be simply written in terms of the three components c_i . As we are primarily interested here in $\langle (\mathbf{e}_\omega \cdot \mathbf{e}_i)^2 \rangle$, we use Eq. 15 for c_i^2 :

$$\left. \frac{dc_i^2}{dt} \right|_{t=0} = 2c_i^2 \left[\lambda_i - \sum_{j=1}^3 \lambda_j c_j^2 \right]. \quad (17)$$

The initial dynamics of alignment is best investigated by averaging over many realizations, and by separating the three components in Eq. (17):

$$\left\langle \frac{dc_1^2}{dt} \right\rangle \Big|_{t=0} = 2\langle c_1^2 c_2^2 (\lambda_1 - \lambda_2) \rangle + 2\langle c_1^2 c_3^2 (\lambda_1 - \lambda_3) \rangle \quad (18)$$

$$\left\langle \frac{dc_2^2}{dt} \right\rangle \Big|_{t=0} = -2\langle c_1^2 c_2^2 (\lambda_1 - \lambda_2) \rangle + 2\langle c_3^2 c_2^2 (\lambda_2 - \lambda_3) \rangle \quad (19)$$

and

$$\left\langle \frac{dc_3^2}{dt} \right\rangle \Big|_{t=0} = -2\langle c_1^2 c_3^2 (\lambda_1 - \lambda_3) \rangle - 2\langle c_2^2 c_3^2 (\lambda_2 - \lambda_3) \rangle \quad (20)$$

The sign of $\langle \frac{dc_i^2}{dt} \rangle|_{t=0}$ is determined solely by the eigenvalues of the rate of strain, with $\lambda_1 \geq \lambda_2 \geq \lambda_3$. We see immediately that $\langle \frac{dc_1^2}{dt} \rangle|_{t=0} > 0$ and $\langle \frac{dc_3^2}{dt} \rangle|_{t=0} < 0$. Thus initially vorticity tends to align with $\mathbf{e}_1(0)$ and to become perpendicular to $\mathbf{e}_3(0)$. By the following argument we also see that $\langle \frac{dc_2^2}{dt} \rangle|_{t=0}$ is smaller in magnitude than the other two components. The first term on the RHS of Eq. 19 is negative and has the same magnitude as the first term on the RHS of Eq. 18, hence this term is negative and smaller in magnitude

than $\langle \frac{dc^2}{dt} \rangle|_{t=0}$. Also, the second term on the RHS of Eq. 19 is positive and has the same magnitude as the second term in the RHS of Eq. 20, therefore this term is smaller than the magnitude of $\langle \frac{dc^2}{dt} \rangle|_{t=0}$. Thus $\langle \frac{dc^2}{dt} \rangle|_{t=0}$ is smaller in magnitude than the other two terms and consequently its evolution is the slowest. This agrees qualitatively with the observations reported before.

The analysis presented above is merely based on the action of strain on the vorticity, which is common to essentially all models aimed at describing the evolution of \mathbf{M} . Comparing more quantitatively the results of the present work with the prediction at short times of more sophisticated models, such as the tetrahedron model¹³ or the Lagrangian stochastic model^{42,43}, requires the determination of several constants in the models, which is beyond the scope of this work. We nevertheless note that in the specific case of the tetrahedron model¹³, the equation of evolution of vorticity reads:

$$\frac{d\omega_i}{dt} - (1 - \alpha)S_{ij}\omega_j = 0 \quad (21)$$

where α , which describes the reduction of nonlinearity, is a parameter that a-priori depends on the scale r_0 . Our observation that the evolution of \mathbf{M} may be self-similar at large Reynolds numbers throughout the inertial range suggests that the parameter of the model are independent of the scale r_0 .

As explained already, an extension of this calculation to later times requires both the knowledge of the interplay between vorticity and the rate of strain^{36,44,45}, as well as the geometry of the tetrahedra. The very good superposition of the correlations $\langle (\mathbf{e}_\omega(t) \cdot \mathbf{e}_1(0))^2 \rangle$ in Fig. 6 corresponding to tetrahedra of different sizes, while r_0 is in the inertial range, is consistent with a description of the dynamics of \mathbf{M} by such a model based on the Restricted Euler approximation or one of its generalizations^{18,39,41,42}. Indeed, on general grounds, \mathbf{M} is expected to behave with scale as $M \propto (\varepsilon/r_0^2)^{1/3}$, so the eigenvalues of the rate of strain λ_i scale as $\lambda_i \propto (\varepsilon/r_0^2)^{1/3}$, which in turn is consistent that the dynamics of alignment proceeds with the characteristic time scale t_0 , as observed before¹⁴ and in this work. More generally, a dynamical equation of the form $\frac{d\mathbf{M}}{dt} \propto \mathbf{M}^2$ immediately suggests that the characteristic time scale of the dynamics should be t_0 , thus suggesting that all the dynamical process should depend on t/t_0 , at least when r_0 is in the inertial range. While our results on the alignment between $\mathbf{e}_\omega(t)$ and $\mathbf{e}_1(0)$ strongly suggests some universal behavior as a function of scale r_0 , it is not settled by the present work whether the dynamics of alignment of vorticity with the other two eigendirections of strain is also self-similar over a range of scales in the inertial scales. It would be very interesting to determine whether a dependence on scale r_0 of the dynamics of \mathbf{M} persists, even at very large Reynolds numbers. These issues are important in many aspects for the modeling of the flow at scales r_0 , in particular concerning the applicability of models based on Restricted Euler, and its generalizations.

C. Alignment of vorticity with the eigenvectors of the rate of strain: conditional statistics

The instantaneous alignment of vorticity with the intermediate eigenvalue of the rate of strain, documented many times before for the true velocity gradient tensor \mathbf{m} , and for the perceived velocity gradient \mathbf{M} (see Fig. 3), results from an averaging over all configurations in the flow, which gives the same statistical weight to any configuration. This may lead to the impression that, in the case of the velocity gradient tensor, the direction of the intermediate eigenvalue of the rate of strain is more important than the largest eigenvalue. However, such casual arguments are deceiving⁴⁶, since the comparatively rare configurations where vorticity is aligned with the largest eigenvalue of the rate of strain may actually contribute more to the dynamics than the frequent contributions, where vorticity is aligned with the intermediate eigenvector. Here we check this argument more quantitatively by studying the alignment weighted by the magnitudes of the rate of strain and vorticity. Again, we study the evolution in the coordinates of $\mathbf{e}_i(0)$, the eigenframe of the rate of strain at some earlier time.

Figure 8 presents $\langle [\mathbf{e}_i(0) \cdot \boldsymbol{\omega}(t)]^2 \rangle / \langle \omega^2(t) \rangle$, *i.e.*, the evolution of the vorticity weighted alignment with $\mathbf{e}_i(0)$ (or the relative components of enstrophy in the $\mathbf{e}_i(0)$ direction). Compared with Fig. 6a, the contribution in $\mathbf{e}_1(0)$ direction is even larger, a consequence of the increase in vorticity due to vortex-stretching in that direction¹⁴. The contribution in $\mathbf{e}_2(0)$, on the other hand, decreases with time, which is to be compared with the nearly constant $\langle [\mathbf{e}_2(0) \cdot \mathbf{e}_\omega(t)]^2 \rangle$ for $t/t_0 \leq 0.2$ in Fig. 6b.

The alignment weighted by the magnitude of eigenvalues of the initial rate of strain is shown in Fig. 9, which calls for the following remarks: (i) The instantaneous alignment is uncorrelated with the magnitude of the rate of strain as $\langle \lambda_i(0)[\mathbf{e}_i(0) \cdot \mathbf{e}_\omega(0)]^2 \rangle \approx \langle \lambda_i(0) \rangle \langle [\mathbf{e}_i(0) \cdot \mathbf{e}_\omega(0)]^2 \rangle$. (ii) The increase of $\langle \lambda_i(0)[\mathbf{e}_i(0) \cdot \mathbf{e}_\omega(t)]^2 \rangle$

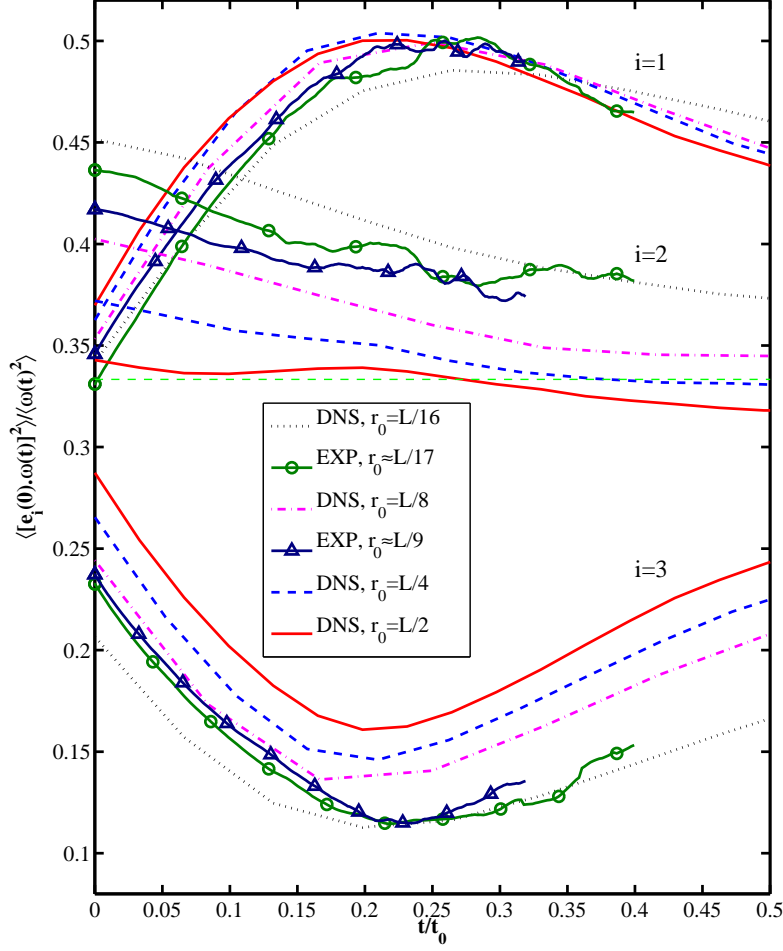


FIG. 8. (Color online) Alignment of $\mathbf{e}_\omega(t)$ with $\mathbf{e}_i(0)$ weighted by vorticity. The averages $\langle [\mathbf{e}_i(0) \cdot \boldsymbol{\omega}(t)]^2 \rangle / \langle \omega^2(t) \rangle$ are shown as a function of t/t_0 for different values of r_0 in the inertial range. The DNS data correspond to $R_\lambda = 170$, and the experiments to $R_\lambda = 350$.

with time in the $\mathbf{e}_1(0)$ direction appears to be uncorrelated with the magnitude of $\lambda_1(0)$ as the same amount of increase (approximately 30%) is achieved in the unconditional statistics $\langle [\mathbf{e}_1(0) \cdot \mathbf{e}_\omega(t)]^2 \rangle$ (see Fig. 6a). Similarly, the contribution in $\mathbf{e}_2(0)$ direction is nearly constant at $t/t_0 \leq 0.2$ before decreases, as $\langle [\mathbf{e}_2(0) \cdot \mathbf{e}_\omega(t)]^2 \rangle$ in Fig. 6b.

The quantity $\langle \lambda_i(0) [\mathbf{e}_i(0) \cdot \boldsymbol{\omega}(t)]^2 \rangle$ measures the evolution of the enstrophy component in the $\mathbf{e}_i(0)$ direction, weighted by the eigenvalues of the rate of strain, $\lambda_i(0)$. At $t = 0$ (instantaneous statistics), the quantity $\langle \lambda_i(0) [\mathbf{e}_i(0) \cdot \boldsymbol{\omega}(0)]^2 \rangle$ reduces to the contribution of the i^{th} eigendirection of \mathbf{S} to the vorticity growth: $\sum_{i=1}^3 \langle \lambda_i(0) [\mathbf{e}_i(0) \cdot \boldsymbol{\omega}(0)]^2 \rangle = \langle \boldsymbol{\omega}(0) \cdot \mathbf{S} \cdot \boldsymbol{\omega}(0) \rangle$, which is the usual vortex stretching. Fig. 10 thus shows the contribution to vortex-stretching from the directions of $\mathbf{e}_1(0)$ and $\mathbf{e}_2(0)$. It is clear that the contribution from $\mathbf{e}_1(0)$ direction increases rapidly with time and is much larger than that from $\mathbf{e}_2(0)$. Moreover, the contribution in $\mathbf{e}_1(0)$, once increased, stays at the larger value for longer time as the statistics conditioned on vorticity or the rate of strain alone (see Figs. 8a and 9a), which indicates that larger rate of strain $\lambda_1(0)$ results in stronger vorticity increase and persists longer.

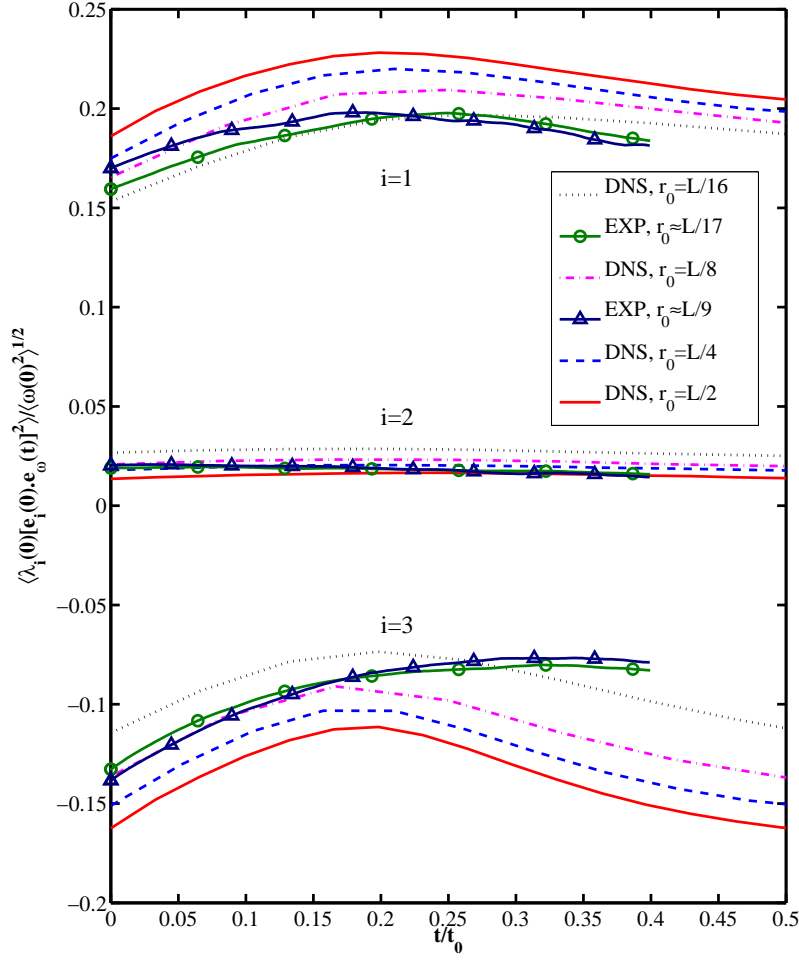


FIG. 9. (Color online) Alignment of $\mathbf{e}_\omega(t)$ with $\mathbf{e}_i(0)$ weighted by strain. The averages $\langle \lambda_i(0) [\mathbf{e}_i(0) \cdot \mathbf{e}_\omega(t)]^2 / \langle \omega^2(0) \rangle^{1/2}$ are shown as a function of t/t_0 for different values of r_0 in the inertial range. The DNS data correspond to $R_\lambda = 170$, and the experiments to $R_\lambda = 350$.

D. Evolution of the intermediate eigenvalue of the rate of strain

In addition to the alignment between vorticity and the eigen-directions of the rate of strain, \mathbf{e}_i , \mathbf{M} is also characterized by the eigenvalues of the rate of strain, in particular by the intermediate one, λ_2 . Here, we consider the normalized value β , defined by Eq. 13. Fig. 11 shows the mean value of β as a function of time t/t_0 , for several values of the tetrahedron size, r_0 . Remarkably, the curves superpose extremely well for $t/t_0 \lesssim 0.25$, as if the evolution were self-similar.

VII. DISCUSSION AND CONCLUSIONS

It is appropriate to stress here that asking questions about \mathbf{M} is merely one way of studying the correlation function of the velocity field $\mathbf{u}(\mathbf{x}, t)$, based on four different spatial points. Although the precise relation between \mathbf{M} and the true velocity gradient tensor, \mathbf{m} , or its coarse-grained generalization is not completely obvious¹⁵, it is our contention that the correlation functions investigated here, based on \mathbf{M} , contain far

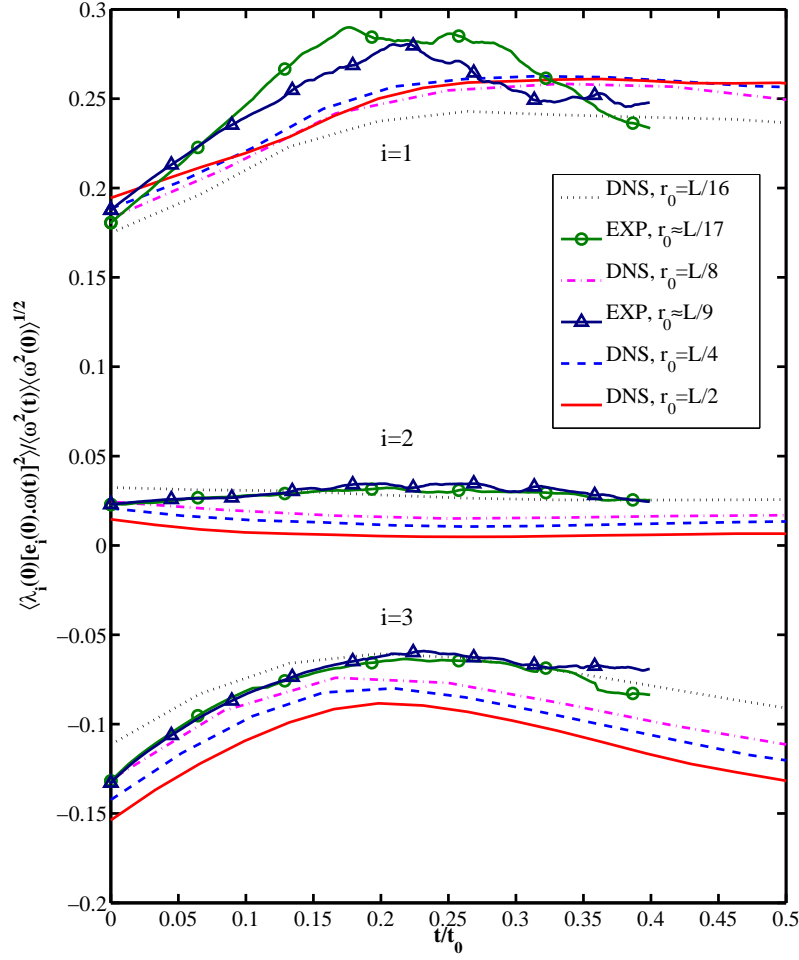


FIG. 10. (Color online) Alignment of $\mathbf{e}_\omega(t)$ with $\mathbf{e}_i(0)$ weighted by both strain and vorticity. The averages $\langle \lambda_i(0) [\mathbf{e}_i(0) \cdot \boldsymbol{\omega}(t)]^2 / \langle \omega^2(t) \rangle \langle \omega^2(0) \rangle^{1/2}$ are shown as a function of t/t_0 for different values of r_0 in the inertial range. The DNS data correspond to $R_\lambda = 170$, and the experiments to $R_\lambda = 350$.

more information than the correlation function of the velocity at two spatial points, such as the structure function, and much can be learned about the turbulent flow by investigating correlation functions at more than two spatial points^{47,48}.

A. Comparison between dissipative and inertial scale dynamics

In the previous sections, the properties of \mathbf{M} have been studied for tetrahedra of size r_0 in the inertial range. It is appropriate to compare these alignment properties with those obtained from the true velocity gradient tensor, \mathbf{m} . We first note that \mathbf{M} reduces to the true velocity gradient tensor when r_0 becomes significantly smaller than the Kolmogorov scale η . Here we report results from the DNS on the evolution of the alignment between the direction of the true vorticity $\mathbf{e}_\omega(t)$ with the eigenvectors $\mathbf{e}_i(0)$ of \mathbf{s} . The statistics characterizing the alignment are shown in Fig. 12. The curves in Fig. 12 and Fig. 6 show strong qualitative similarities. They differ only in the scaling of the t -axis. We find that in the dissipative range the characteristic time scale for alignment between vorticity and strain is $\sim 2 - 3\tau_K$, which coincides with

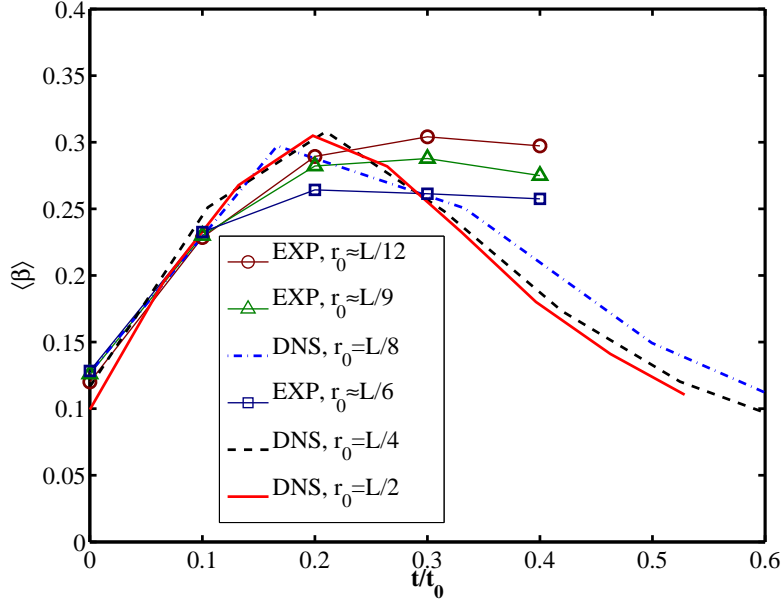


FIG. 11. (Color online) Evolution of $\langle \beta \rangle$, the mean of the normalized intermediate eigenvalue of strain. With time rescaled with t_0 , the curves corresponding to different values of r_0 collapse very well. The DNS data correspond to $R_\lambda = 170$, and the experiments to $R_\lambda = 350$.

the correlation time of the rate of strain tensor^{49,50}, where $\tau_K \equiv (\nu/\varepsilon)^{1/2}$ is the Kolmogorov time scale. Remarkably, the strongest alignment of $\mathbf{e}_\omega(t)$ with $\mathbf{e}_1(0)$ in the dissipative range is as strong as it is in the inertial one: compare Fig. 12 and Fig. 6(a). The tendency of $\mathbf{e}_\omega(0)$ to align with $\mathbf{e}_2(0)$, and to be perpendicular to $\mathbf{e}_3(0)$ is stronger in the dissipative range than in the inertial range, as shown also in Fig. 3(c). Thus, the properties of alignment between $\mathbf{e}_\omega(t)$ and $\mathbf{e}_i(0)$ for \mathbf{M} when r_0 is in the inertial range are quite similar with the properties of the true velocity gradient tensor \mathbf{m} . Similar observations were reported in another very recent numerical study⁴³.

B. Fixed shape tetrahedra

The coupling between the dynamics of \mathbf{M} and the geometry of the set of points has been postulated to be a crucial ingredient in any effort to properly understand the dynamics of the velocity gradient tensor^{13,18,42}. The recent experimental and numerical work¹⁴ effectively demonstrates that the properties of alignment of vorticity with the eigenvalues of the rate of strain are strongly dependent on the deformation of the tetrahedra. In this context it is worth to ask how the dynamics of alignment is modified, if instead of following Lagrangian tetrahedra that are deformed by the flow, one considers tetrahedra of *fixed* shape and size. To analyze this we followed numerically one single tracer particle, and used it as the center of mass of an isotropic tetrahedron with a fixed size and arbitrary orientation. A similar approach was used before⁵¹ for fixed volumes following Lagrangian particles. For values of r_0 much smaller than the Kolmogorov length scale, η , the velocity gradient tensor obtained using this construction reduces to the true velocity gradient tensor \mathbf{m} , whose properties are illustrated in Fig. 12.

Fig. 13 shows the evolution of the alignment of $\mathbf{e}_\omega(t)$ with the eigenvectors of the rate of strain $\mathbf{e}_i(0)$ for the velocity gradient tensor obtained from *fixed shape* tetrahedra. Comparing Fig. 6 and Fig. 13 reveals some strong quantitative differences. The tendency $\mathbf{e}_\omega(t)$ to align with $\mathbf{e}_1(0)$, as measured by the increase of $\langle (\mathbf{e}_\omega(t) \cdot \mathbf{e}_1(0))^2 \rangle$, is much weaker for fixed-shape tetrahedra than for deformable tetrahedra. Similarly, the tendency of $\mathbf{e}_\omega(t)$ to become more perpendicular to $\mathbf{e}_3(0)$ is much reduced. We also notice that the time scale of the alignment process is much longer for fixed-shape tetrahedra. Moreover, the degrees of alignment for fixed-shape tetrahedra (Fig. 13) are much weaker than for the dissipative range.

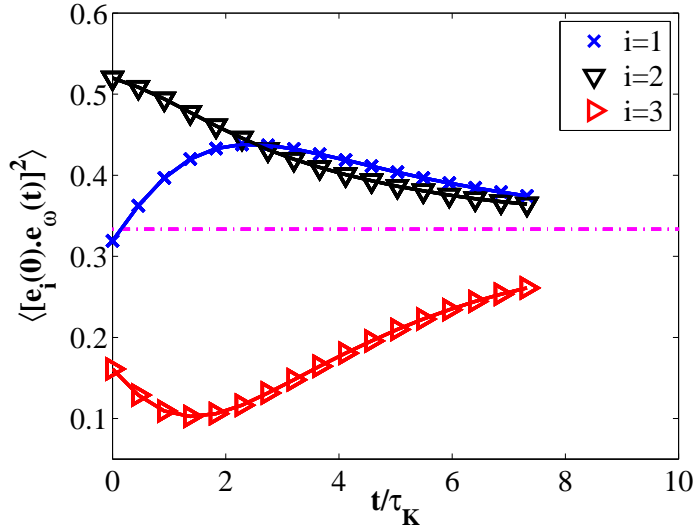


FIG. 12. (Color online) Alignment between $\mathbf{e}_\omega(t)$ and $\mathbf{e}_i(0)$ for the true velocity gradient tensor \mathbf{m} , obtained from DNS ($R_\lambda = 170$). The averages $\langle [e_i(0) \cdot e_\omega(t)]^2 \rangle$ for $i = 1, 2$ and 3 , are indicated by crosses, downwards pointing, and right pointing triangles. The time is normalized by the Kolmogorov time scale, $\tau_K = (\nu/\varepsilon)^{1/2}$. The observed evolutions of the alignment of $\mathbf{e}_\omega(t)$ and $\mathbf{e}_i(0)$ are qualitatively very similar to what is shown in Fig. 6 for tetrahedra with size r_0 in the inertial range.

The results shown in Fig. 13 thus demonstrate a very important feature: the properties of alignment of \mathbf{M} , constructed with properly deformable tetrahedra are much closer to those of the true velocity gradient tensor, than those obtained with fixed shape tetrahedra. The coupling between the dynamics of \mathbf{M} and of the geometry is crucial to properly understand and model fluid motion.

C. Summary

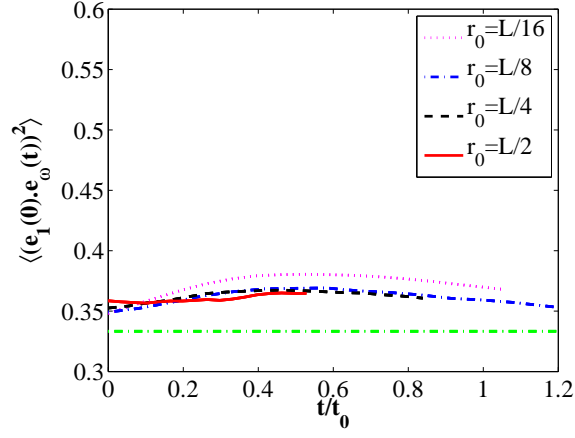
To sum up, we have investigated systematically the perceived velocity gradient \mathbf{M} from the point of view of alignment between vorticity and the rate of strain, using both DNS at $R_\lambda = 170$, over the entire range of scales, and experiments at a higher Reynolds numbers ($R_\lambda = 350$) but over a more restricted range of scales in the inertial range. Our results generalize our recent work¹⁴, which focused on the alignment between vorticity and the eigenvector \mathbf{e}_1 corresponding to the largest stretching.

We found that strong deformation of tetrahedra, leading to the formation of flattened, almost coplanar configurations, occurs over a time scale of the order $t_0/4$, which is comparable to the time scale characterizing the alignment of vorticity with the eigenvector $\mathbf{e}_1(0)$ of the strain, corresponding to the largest eigenvalue, $\sim t_0/5$, see Fig. 6(a). We note in this respect that during this time, the relative orientation of the vectors $\mathbf{e}_\omega(t)$ and $\mathbf{e}_2(0)$ remains nearly constant, see Figs. 6(b) and 7(b), (e), and (h).

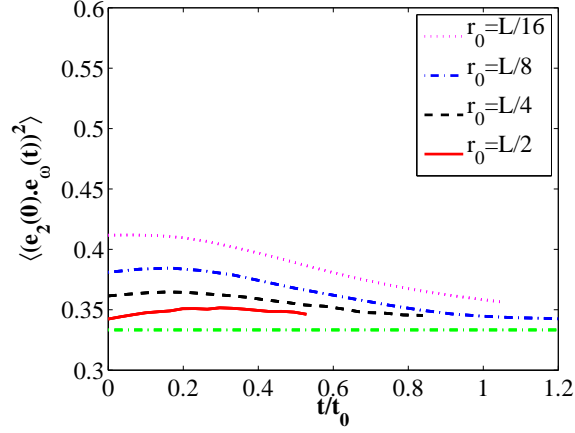
Whereas the dynamics leading to alignment between ω and \mathbf{e}_1 has been found to be essentially self-similar¹⁴ over the whole range of scales *and* Reynolds numbers considered, the self-similarity of the statistical properties of the angle between ω and the other two eigendirections of the rate of strain is only observed at the largest Reynolds number studied here, $R_\lambda = 350$. At small Reynolds numbers, $R_\lambda \leq 170$, we found a systematic dependence on the size r_0 of the tetrahedra of the alignment of vorticity and the rate of strain at the *same* time. We also observed that the evolution of the angle between vorticity and the second and third eigenvalues of the rate of strain does not simply reduce to a simple function of t/t_0 . In any event, the dynamics proceed with a characteristic time scale of order $\sim t_0/5$.

For the range of Reynolds numbers considered here, the picture that emerges from the study of \mathbf{M} reflects the properties in the dissipative scale in terms of alignment of vorticity and strain eigenvectors. The characteristic time of evolution in the dissipative scale is $\sim 2 - 3\tau_K$.

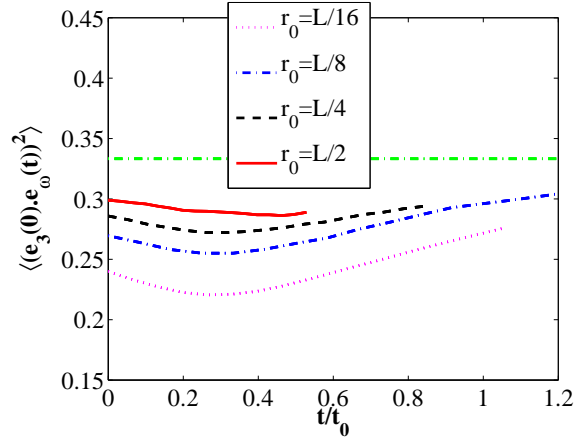
Future studies will be devoted to a more systematic comparison with modeling, both in terms of the tetrahedron model¹³, and in terms of the arguments developed in our recent work¹⁴.



(a)



(b)



(c)

FIG. 13. (Color online) Alignment between $\mathbf{e}_\omega(t)$ and $\mathbf{e}_i(0)$ measured with isotropic tetrahedra of fixed shapes and size r_0 , obtained from DNS at $R_\lambda = 170$. The averages $\langle [\mathbf{e}_i(0) \cdot \mathbf{e}_\omega(t)]^2 \rangle$ for $i = 1$ (a), 2 (b) and 3 (c), as a function of t/t_0 , are shown for several values of r_0 , all in the inertial range. The tendency of $\mathbf{e}_\omega(t)$ to align with $\mathbf{e}_1(0)$, and to become perpendicular to $\mathbf{e}_3(0)$, are much weaker than with tetrahedra freely advected with the flow (compare with Fig. 6), or with the true velocity gradient tensor (compare with Fig. 12).

ACKNOWLEDGEMENT

We are very thankful to B. Lüthi, B. Shraiman, E. Siggia and A. Tsinober for stimulating discussions, and to L. Chevillard and C. Meneveau for communicating to us reference⁴³, and for freely sharing their insight. AP thanks IDRIS for providing the computation resources and the ANR for financial support through the contract TEC2. HX is grateful to the Deutsche Forschungsgemeinschaft for support through the grant XU 91/3-1. We thank the Max Planck Society for support. This research was conducted in part at the Kavli Institute for Theoretical Physics at Santa Barbara, CA (supported by the US National Science Foundation under Grant No. NSF PHY05-51164), the Kavli Institute for Theoretical Physics China at Beijing (supported by the Project of Knowledge Innovation Program (PKIP) of the Chinese Academy of Sciences under Grant No. KJCX2.YW.W10) and received additional support from the the European COST Action MP0806.

- ¹G. I. Taylor, "Production and dissipation of vorticity in a turbulent fluid," *Proc. R. Soc. Lond.*, **A164**, 15–23 (1938).
- ²A. Pumir and E. D. Siggia, "Collapsing solutions to the 3d Euler equations," *Phys. Fluids A*, **2**, 220–241 (1990).
- ³W. Pauls, T. Matsumoto, U. Frisch, and J. Bec, "Nature of complex singularities for the 2d Euler equation," *Physica D*, **219**, 40–59 (2006).
- ⁴J. D. Gibbon, M. Bustamante, and R. M. Kerr, "The three-dimensional Euler equations: singular or non-singular?" *Non-linearity*, **21**, T123–129 (2008).
- ⁵J. Schumacher, K. R. Sreenivasan, and V. Yakhot, "Asymptotic exponents from low-Reynolds-number flows," *New J. Phys.*, **9**, 89 (2007).
- ⁶A. Tsinober, E. Kit, and T. Dracos, "Experimental investigation of the field of velocity gradients in turbulent flows," *J. Fluid Mech.*, **242**, 169–192 (1992).
- ⁷F. van der Bos, B. Tao, C. Meneveau, and J. Katz, "Effects of small-scale turbulent motions on the filtered velocity gradient tensor as deduced from holographic particle image velocimetry measurements," *Phys. Fluids*, **14**, 2456–2474 (2002).
- ⁸B. W. Zeff, D. D. Lanterman, R. McAllister, R. Roy, E. H. Kostelich, and D. P. Lathrop, "Measuring intense rotation and dissipation in turbulent flows," *Nature*, **421**, 146–149 (2003).
- ⁹B. Lüthi, A. Tsinober, and W. Kinzelbach, "Lagrangian measurements of vorticity dynamics in turbulent flow," *J. Fluid Mech.*, **528**, 87–118 (2005).
- ¹⁰J. M. Wallace, "Twenty years of experimental and direct numerical simulation access to the velocity gradient tensor: What have we learned about turbulence?" *Phys. Fluids*, **21**, 021301 (2009).
- ¹¹J. M. Wallace and P. V. Vukoslavčević, "Measurement of velocity gradient tensor in turbulent flows," *Annu. Rev. Fluid Mech.*, **42**, 157–181 (2010).
- ¹²O. R. Buxton, S. Laizet, and B. Ganapathisubramani, "The interaction between strain-rate and rotation in shear flow turbulence from inertial range to dissipative length scales," *Phys. Fluids*, **23**, 061704 (2011).
- ¹³M. Chertkov, A. Pumir, and B. I. Shraiman, "Lagrangian tetrad dynamics and the phenomenology of turbulence," *Phys. Fluids*, **11**, 2394–2410 (1999).
- ¹⁴H. Xu, A. Pumir, and E. Bodenschatz, "The pirouette effect in turbulent flows," *Nat. Phys.*, **7**, 709–712 (2011).
- ¹⁵B. Lüthi, S. Ott, J. Berg, and J. Mann, "Lagrangian multi-particle statistics," *J. Turbul.*, **8**, 45 (2007).
- ¹⁶E. D. Siggia, "Invariants for the one-point vorticity and strain rate correlation functions," *Phys. Fluids*, **24**, 1934–1936 (1981).
- ¹⁷W. T. Ashurst, A. R. Kerstein, R. M. Kerr, and C. H. Gibson, "Alignment of vorticity and scalar gradient with strain rate in simulated navier-stokes turbulence," *Phys. Fluids*, **30**, 2343–2353 (1987).
- ¹⁸C. Meneveau, "Lagrangian dynamics and models of the velocity gradient tensor in turbulent flows," *Annu. Rev. Fluid Mech.*, **43**, 219–245 (2011).
- ¹⁹G. I. Taylor, "The statistical theory of isotropic turbulence," *J. Aeronaut. Sci.*, **4**, 311–315 (1937).
- ²⁰W. H. Press, S. A. Teukolsky, W. T. Vetterling, and B. P. Flannery, *Numerical Recipes in C: The Art of Scientific Computing* (Cambridge University Press, 1992).
- ²¹H. Xu, N. T. Ouellette, and E. Bodenschatz, "Evolution of geometric structures in intense turbulence," *New J. Phys.*, **10**, 013012 (2008).
- ²²J. F. Hackl, P. K. Yeung, and B. L. Sawford, "Multi-particle and tetrad statistics in numerical simulations of turbulent dispersion," *Phys. Fluids*, **23**, 065103 (2011).
- ²³A. La Porta, G. A. Voth, A. M. Crawford, J. Alexander, and E. Bodenschatz, "Fluid particle accelerations in fully developed turbulence," *Nature*, **409**, 1017–1019 (2001).
- ²⁴G. A. Voth, A. La Porta, A. M. Crawford, J. Alexander, and E. Bodenschatz, "Measurement of particle accelerations in fully developed turbulence," *J. Fluid Mech.*, **469**, 121–160 (2002).
- ²⁵N. T. Ouellette, H. Xu, and E. Bodenschatz, "A quantitative study of three-dimensional Lagrangian particle tracking algorithms," *Exp. Fluids*, **40**, 301–313 (2006).
- ²⁶H. Xu, "Tracking Lagrangian trajectories in position-velocity space," *Meas. Sci. Tech.*, **19**, 075105 (2008).
- ²⁷N. Mordant, A. M. Crawford, and E. Bodenschatz, "Experimental Lagrangian acceleration probability density function measurement," *Physica D*, **193**, 245–251 (2004).
- ²⁸H. Xu, N. T. Ouellette, D. Vincenzi, and E. Bodenschatz, "Acceleration correlations and pressure structure functions in high-Reynolds number turbulence," *Phys. Rev. Lett.*, **99**, 204501 (2007).
- ²⁹S. B. Pope, *Turbulent Flows* (Cambridge University Press, Cambridge, England, 2000).
- ³⁰Q. Nie and S. Tanveer, "Recovering isotropic statistics in turbulence simulations: the kolmogorov 4/5th law," *Proc. R. Soc. Lond. A*, **455**, 1615 (1999).
- ³¹M. A. Taylor, S. Kurien, and G. L. Eyink, "Recovering isotropic statistics in turbulence simulations: the kolmogorov 4/5th law," *Phys. Rev. E*, **68**, 026310 (2003).

- ³²A. Pumir, “A numerical study of pressure fluctuations in three-dimensional, incompressible, homogeneous, isotropic turbulence,” *Phys. Fluids*, **6**, 2071–2083 (1994).
- ³³P. K. Yeung and S. B. Pope, “An algorithm for tracking fluid particles in numerical simulations of homogeneous turbulence,” *J. Comput. Phys.*, **79**, 373–416 (1988).
- ³⁴A. Pumir, B. I. Shraiman, and M. Chertkov, “Geometry of Lagrangian dispersion in turbulence,” *Phys. Rev. Lett.*, **85**, 5324–5327 (2000).
- ³⁵L. Biferale, G. Boffetta, A. Celani, B. J. Devenish, A. Lanotte, and F. Toschi, “Multiparticle dispersion in fully developed turbulence,” *Phys. Fluids*, **17**, 111701 (2005).
- ³⁶Z.-S. She, E. Jackson, and S. A. Orszag, “Structure and dynamics of homogeneous turbulence,” *Proc. R. Soc. Lond. A*, **434**, 101–124 (1991).
- ³⁷R. Betchov, “An inequality concerning the production of vorticity in isotropic turbulence,” *J. Fluid Mech.*, **1**, 497–504 (1956).
- ³⁸T. Tennekes and J. L. Lumley, *A First Course in Turbulence* (The MIT Press, Cambridge, USA, 1972).
- ³⁹P. Vieillefosse, “Local interaction between vorticity and shear in a perfect incompressible fluid,” *J. Physique*, **43**, 837–842 (1982).
- ⁴⁰P. Vieillefosse, “Internal motion of a small element of fluid in an inviscid flow,” *Physica A*, **125**, 150–162 (1984).
- ⁴¹B. J. Cantwell, “Exact solution of a restricted Euler equation for the velocity gradient tensor,” *Phys. Fluids A*, **4**, 782–793 (1992).
- ⁴²L. Chevillard and C. Meneveau, “Lagrangian dynamics and statistical geometric structure of turbulence,” *Phys. Rev. Lett.*, **97**, 174501 (2006).
- ⁴³L. Chevillard and C. Meneveau, “Lagrangian time correlations of vorticity alignments in isotropic turbulence: observations and model predictions,” *Phys. Fluids*, **23**, 101704 (2011).
- ⁴⁴E. Dresselhaus and M. Tabor, “The kinematics of stretching and alignment of material elements in general flow fields,” *J. Fluid Mech.*, **236**, 415–444 (1991).
- ⁴⁵K. K. Nomura and G. K. Post, “The structure and dynamics of vorticity and rate of strain in incompressible homogeneous turbulence,” *J. Fluid Mech.*, **377**, 65–97 (1998).
- ⁴⁶A. Tsinober, *An Informal Conceptual Introduction to Turbulence* (Springer, Berlin, 2009).
- ⁴⁷L. Mydlarski, A. Pumir, B. I. Shraiman, E. D. Siggia, and Z. Warhaft, “Structures and multipoint correlators for turbulent advection: Predictions and experiments,” *Phys. Rev. Lett.*, **81**, 4373–4376 (1998).
- ⁴⁸B. I. Shraiman and E. D. Siggia, “Scalar turbulence,” *Nature*, **405**, 639–646 (2000).
- ⁴⁹P. K. Yeung, S. B. Pope, E. A. Kurth, and A. G. Lamorgese, “Lagrangian conditional statistics, acceleration and local relative motion in numerically simulated isotropic turbulence,” *J. Fluid Mech.*, **582**, 399–422 (2007).
- ⁵⁰A. Pumir and M. Wilkinson, “Orientation statistics of small particles in turbulence,” *New J. Phys.*, **13**, 093030 (2011).
- ⁵¹C. Meneveau and T. S. Lund, “On the lagrangian nature of the turbulence energy cascade,” *Phys. Fluids*, **6**, 2820–2825 (1994).